

Article

Effect of Engine Design Parameters on the Climate Impact of Aircraft: A Case Study Based on Short-Medium Range Mission

Harjot Singh Saluja ¹, Feijia Yin ^{1,*}, Arvind Gangoli Rao ¹ and Volker Grewe ^{1,2}

¹ Faculty of Aerospace Engineering, Delft University of Technology, Kluyverweg 1, 2629 HS Delft, The Netherlands; h.s.saluja@tudelft.nl (H.S.S.); a.gangolirao@tudelft.nl (A.G.R.); volker.grewe@dlr.de (V.G.)

² Deutsches Zentrum für Luft- und Raumfahrt, Institut für Physik der Atmosphäre, Oberpfaffenhofen, 82234 Weßling, Germany

* Correspondence: f.yin@tudelft.nl

Abstract: The climate impact of aviation is considerably different from that of other transport modes. The turbofan engine's efficiency can be increased by increasing the Operating Pressure Ratio (OPR), bypass ratio (BPR) and Turbine Inlet Temperature (TIT), thereby reducing CO₂ and H₂O emissions. However, this may have an adverse effect on the secondary emissions, such as NO_x, soot, etc. Taking a holistic view in evaluating the climate impact of engine development trends considering all the climate forcers is imperative for design trends in the future. This research investigates the impact of some key engine design parameters on climate. The emission changes due to design variations in the CFM56-5B are estimated using in-house engine performance and emission prediction tools. Accordingly, the changes in the species' Average Temperature Response for 100 years (ATR₁₀₀) are analyzed using a climate assessment tool, AirClim. The results show that the overall climate impact increases by 40% when increasing OPR from 25 to 40. Meanwhile, the Twin Annular Premixed Swirler (TAPS-II) combustor reduces the total ATR₁₀₀ drastically, in the range of 52–58%, due to lean combustion.

Keywords: turbofan engine design; aviation climate impact; aircraft emissions; combustion technology



Citation: Saluja, H.S.; Yin, F.; Gangoli Rao, A.; Grewe, V. Effect of Engine Design Parameters on the Climate Impact of Aircraft: A Case Study Based on Short-Medium Range Mission. *Aerospace* **2023**, *10*, 1004. <https://doi.org/10.3390/aerospace10121004>

Academic Editor: Cristian Foça

Received: 3 October 2023

Revised: 17 November 2023

Accepted: 22 November 2023

Published: 29 November 2023



Copyright: © 2023 by the authors. Licensee MDPI, Basel, Switzerland. This article is an open access article distributed under the terms and conditions of the Creative Commons Attribution (CC BY) license (<https://creativecommons.org/licenses/by/4.0/>).

1. Introduction

The impact of global aviation emissions in 2018 was estimated to be 3.5% of the total anthropogenic Effective Radiative Forcing (ERF) [1]. The aviation industry had been growing rapidly until the COVID-19 pandemic. The International Civil Aviation Organization's (ICAO) post-COVID-19 forecasts indicate that aviation will recover with an average growth rate of 3.6% until 2050 (<https://www.icao.int/sustainability/Pages/Post-Covid-Forecasts-Scenarios.aspx> (accessed on 28 September 2023)). As air traffic is expected to grow in the future, aviation's contribution to global climate change will be aggravated. Developing effective climate mitigation measures for the aviation sector is imperative.

Apart from the direct global warming effect from CO₂, a major contribution to aviation's climate impact is due to various non-CO₂ effects. These non-CO₂ effects include the direct water vapor (H₂O) emission effect [2], the indirect NO_x emission effect via the ozone formation in the troposphere and the lower-most stratosphere, methane depletion [3,4], and the subsequent primary-mode ozone (PMO) effects, i.e., reduced ozone production due to the reduced CH₄ background concentrations [5], and the contrail effect [6–9]. Furthermore, non-volatile Particulate Matter (nvPM) from aircraft engines also has a greenhouse effect due to the absorption of outgoing longwave radiation [1]. In addition, nvPM also acts as ice nuclei, forming ice crystals under favorable atmospheric conditions, which affects the characteristics of contrails (e.g., lifetime and radiative effects), hence the actual climate impact of contrails [10]. Overall, these non-CO₂ effects contribute approximately two-thirds of the total aviation's net positive ERF [1]. While the impact of well-mixed greenhouse gases like

CO₂ is location-independent [11], the impact of non-CO₂ emissions depends on a variety of factors, such as the geographical location, altitude, time of emissions (e.g., day/night for contrails) and the local weather conditions [12,13]. Therefore, the local climate impact of aviation is not uniform across the earth, which needs to be considered for assessment.

Various efforts have been undertaken by organizations globally to address the challenge of the growing climate impact of aviation. Ambitious climate goals have been set up, which require rapid development and the adaptation of disruptive technologies. For instance, the Advisory Council for Aviation Research and Innovation in Europe (ACARE) has set the Flightpath 2050 targets to reduce the per passenger-km CO₂ emissions by 75% and the NO_x emissions by 90% by 2050 relative to a typical new aircraft in the year 2000 [14]. The ICAO has introduced the Carbon Offsetting and Reduction Scheme for International Aviation (CORSIA), which aims to realize the carbon-neutral growth of the aviation sector. Grewe et al. (2021) [15] analyzed the climate impacts of different scenarios concerning measures like CORSIA and Flightpath 2050. By allowing aviation a 5% share of the goals of the Paris Agreement, they demonstrated that the Flightpath 2050 emission goals are in line with the target of limiting warming to 2 °C above pre-industrial levels [16], though they are not completely climate-neutral. In addition, it was also pointed out that with the currently expected technology enhancements, the emission goals are unlikely to be achieved.

However, simultaneously reducing CO₂ and NO_x from the turbofan engine has been challenging because of the technological trade-off between fuel burn and NO_x emissions [17–19]. One of the engine design trends has been to increase the Overall Pressure Ratio (OPR) combined with the increase in Turbine Inlet Temperature (TIT) to reduce the fuel burn, as can be seen in Figure 1, taken from Yin and Rao (2017) [18]. As stringent emission assessments were undertaken, it became apparent that the engine cycle development trend of pushing towards a high-pressure ratio resulted in a NO_x penalty unless low NO_x combustion techniques were applied [20,21]. Given such trade-offs, Freeman et al. (2018) [22] showed that to reach the “break-even” point at the overall RF, a 20% NO_x reduction would only allow a 0.5% increase in CO₂. However, the actual sensitivity of NO_x to CO₂ in a state-of-the-art aircraft system has been virtually left out of the discussion. Furthermore, despite the complex nature of the nvPM formation process, in general, the nvPM emissions increase along with the combustor inlet temperature [23]. This implies a trade-off between CO₂ and nvPM, and thus further trade-offs between the climate impact of CO₂ and non-CO₂ effects. Previous research proposed novel engine cycles to reduce the emissions of aircraft, and therefore the consequent environmental impact. Examples include Water-Enhanced Turbofans (WETs) [24] and composite engine cycle [25].

Apart from engine cycle development, combustion technology is considered significant in affecting NO_x and nvPM emissions [26]. The state-of-the-art combustion technology in use can be categorized into rich-burn (represented by rich-burn, quick-quench, lean-burn (RQL) combustion technology) and lean burn (LB) (represented by the TAPS combustion technology [27] applied in GEnx and LEAP engines). Compared to RQL combustion, the TAPS combustion technology is expected to reduce both NO_x and nvPM emissions substantially, which is beneficial from a climate impact point of view. Having a quantitative measure of such trade-offs in mind is essential for future engine design aspiring towards climate neutrality.

This paper aims to evaluate the climate impact of turbofan engine design in terms of cycle development and combustion technologies over time, with the Average Temperature Response over 100 years (ATR₁₀₀) being the climate metric. The analysis is carried out by varying two fundamental parameters for turbofan engines: the OPR and the TIT. Therefore, depending on these two parameters, the variation of fuel consumption, NO_x emissions, nvPM particle number, and climate response in ATR₁₀₀ are examined in detail. Towards this end, we applied a complete model chain including an aircraft and engine performance model, emission models for NO_x and nvPM prediction, and a state-of-the-art climate assessment model, AirCilm [5,28]. Section 2 of the paper elaborates on the methodology of

the research. Section 3 then presents the main findings of the research. Section 4 concludes the research findings and discusses further considerations of the analysis.

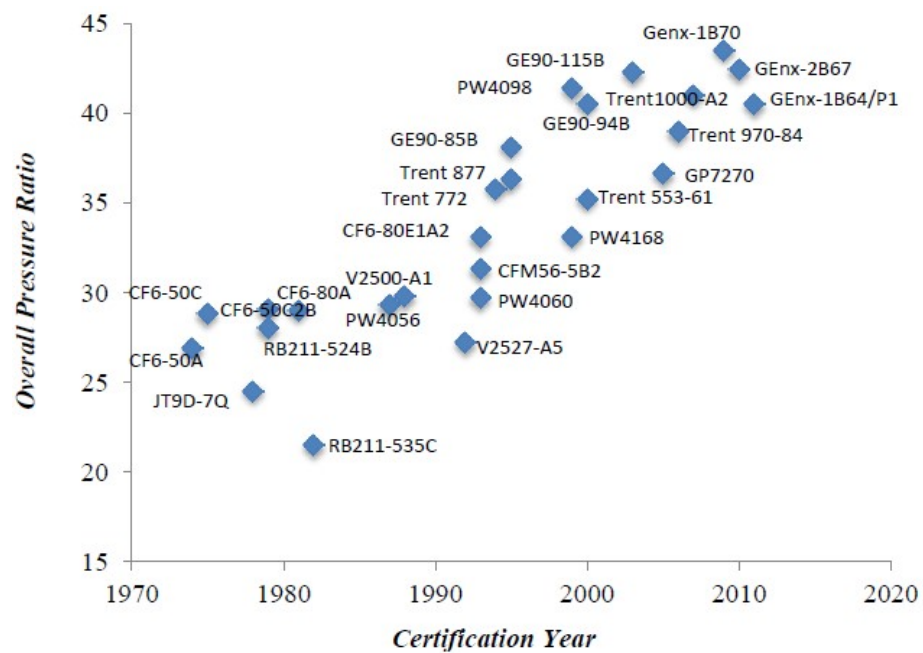


Figure 1. An overview of engine pressure ratio development over the years [18] (reprinted with permission).

2. Methodology

Figure 2 shows an overview of the model chain for this research. The methodology relies on a complete model chain consisting of aircraft and engine performance models, emissions models developed in-house for NO_x and nvPM predictions and based on the P3-T3 method [29], and a state-of-the-art climate assessment model, AirClim [5,28]. There are three aspects of the climate impact evaluation of aviation technologies: the technology itself, the flight planning in which the said technology is applied, and the related atmospheric response. To determine the performance of the considered technology in terms of fuel consumption and emissions, we consider the various models, as shown in the figure. The flight planning is represented by the emission inventory based on these performance parameters, and the atmospheric response given by AirClim. For the emission inventory, we consider a total of 60 city pairs where A320 flights were operational in North America and Europe. The geographical location data for these city pairs, in the form of longitude–latitude pair, were obtained from the OpenSky Network [30], which is used to calculate the cruise distance. The number of passengers was taken to be 150, with 90 kg each, including baggage weight, giving the total passenger payload weight as 13.5 tons. For each city pair, the aircraft performance model along with the engine model calculates the thrust requirement during cruising, with the cruise altitude, h_{cruise} , being fixed at 33,000 ft, and the Mach no. at 0.78. The station thermodynamic data from the engine model are used to calculate the NO_x and nvPM emissions from the in-house models. The geographical location data, fuel consumption, emissions, flight altitude and the frequency of flights for all the city pairs combine to form the emission inventory. The emission inventory serves as an input to AirClim [5,28], which then calculates the ATR_{100} .

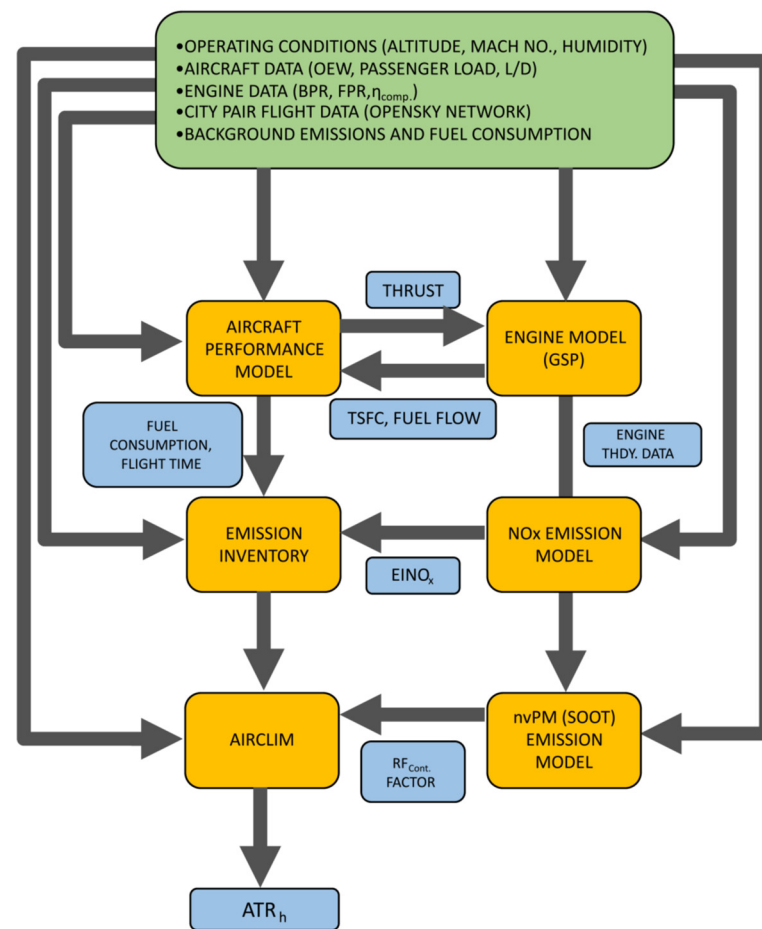


Figure 2. The overview of the modeling chain implemented in this research. The contents in green at the top represent the various boundary/operating conditions, those in yellow represent the various models, and those in blue represent the relevant parameters and outputs of interest.

2.1. Aircraft Performance Model

While there are aircraft performance tools available [31], for this research, a simple aircraft performance model was developed in-house, allowing better integration with the engine performance model, which is described in the subsequent section. The aircraft performance model uses the Breguet Range equation principles to estimate the cruise thrust requirement. As the aircraft weight reduces during cruising, the thrust requirement decreases at a constant Mach no. In this research, the average cruise thrust for the aircraft ($F_{avg.aircraft}$) was calculated using the simple force–balance equation for aircraft cruise [32], shown in Equations (1) and (2):

$$F_{avg.aircraft} = \frac{W_{avg.} \cdot g}{(L/D)} \quad (1)$$

where

$$W_{avg.} = \frac{W_{start} + W_{end}}{2} \quad (2)$$

W_{start} is the aircraft weight at the beginning of cruising, consisting of the operating empty weight (OEW), the apparent payload weight ($W_{app.payload}$, composed of the payload weight and the total fuel for the descent, approach phases, and the reserves), and the required cruise fuel ($W_{f.cruise}$). W_{end} is the aircraft weight at the cruise end, consisting only of the OEW and the $W_{app.payload}$. L/D is the lift-to-drag ratio. The $W_{app.payload}$ is obtained from the actual payload using a payload multiplication factor. With the average cruise

thrust and the cruise fuel consumption, the cruise time, t_{cruise} , could be calculated from the definition of thrust-specific fuel consumption (TSFC) [32], shown in Equation (3):

$$t_{cruise} = \frac{W_{f,cruise}}{TSFC \cdot F_{avg.aircraft}} \quad (3)$$

where TSFC is the thrust-specific fuel consumption. The cruise distance, d_{cruise} , could be determined using a simple distance–time relation for a given cruise speed.

The key model outputs, $F_{avg.engine}$, t_{cruise} and d_{cruise} , obtained using this approach were compared with results from a commercial aircraft performance tool, PIANO-X (<https://www.lissys.uk/PianoX.html> (accessed on July 2023)). Three different aircraft were simulated in PIANO-X for their respective design range and standard payload conditions, as defined in PIANO-X. The details of these PIANO-X simulations are given in Appendix A.1. The comparison of the resultant aircraft performance parameters with those from PIANO-X is shown in Figure 3. Overall, the relative difference was $\pm 2.5\%$ with respect to PIANO-X results.

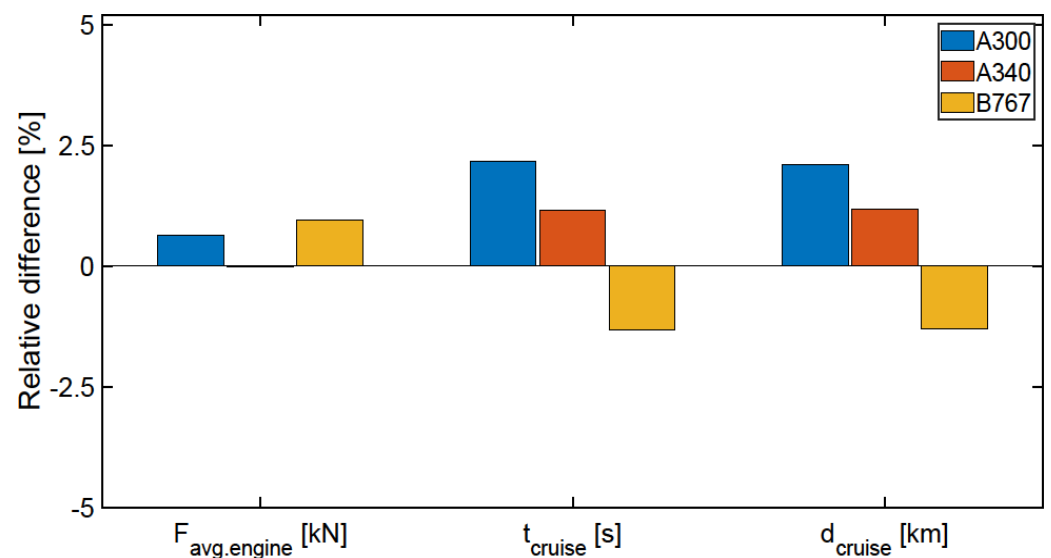


Figure 3. Relative difference of key aircraft performance parameters calculated by the in-house model with respect to PIANO-X output.

Further, PIANO was also used to determine the payload multiplication factor. Several simulations were carried out for different aircraft, and this factor was found to range from 1.17 to 1.25. In this research, this factor is assumed to be 1.22.

2.2. Engine Performance Model

In this research, engine modeling was carried out in the Gas Turbine Simulation Program (GSP) [33]. The engine model was coupled with the aircraft performance model, described previously, via the GSP API module, enabling automated engine performance calculations. The average engine cruise thrust, $F_{avg.engine}$, along with the h_{cruise} and the Mach no., serve as inputs in GSP.

The CFM56-5B4/P (ICAO UID: 3CM026) was taken as the baseline engine model, for which the pressure ratio, the bypass ratio, and the fuel and emission characteristics for the landing and take-off (LTO) cycle were obtained from the ICAO engine emissions databank (<https://www.easa.europa.eu/domains/environment/icao-aircraft-engine-emissions-databank> (accessed on July 2023)).

Initially, GSP determines a design point and then calculates the output for off-design conditions. For this analysis, the design point was taken to be at the rated thrust setting at static sea-level (SLS) conditions. The intake air mass flow rate \dot{w}_a was obtained as

377.75 kg/s to match the rated thrust under the SLS condition, and the TIT was found to be 1535 K. It should be noted that the design point does not refer to the condition for which the turbofan engine is designed; rather, design point is a reference operating condition where information about the engine parameters is known beforehand from the ICAO databank.

Once the engine was modeled under the design conditions, the cruise condition, i.e., the off-design condition, was simulated for each city pair. The resultant TSFC and cruise fuel flow rate $\dot{W}_{f,cruise}$ were then fed back to the performance model to determine the total cruise fuel consumption ($W_{f,cruise}$) and the t_{cruise} . Further, the engine's thermodynamic data from GSP were used in the emission models as input.

2.3. Emission Models

This section describes the emission models implemented in this study. The two main products of complete combustion, CO₂ and H₂O are proportional to the fuel burn. These can be calculated using Equation (4) [34]:

$$W_{species,cruise} = EI_{species} \cdot W_{f,cruise} \quad (4)$$

where $W_{species,cruise}$ is the weight of the emission species in kg, and $EI_{species}$ is the emission index (EI) of the species in kg (species)/kg fuel. The EIs for CO₂ and H₂O are taken to be 3.15 kg(CO₂)/kg fuel and 1.25 kg(H₂O)/kg fuel.

Estimating the non-CO₂ emissions of NO_x and nvPM is not straightforward. These are largely dependent on the combustion parameters and power settings. For NO_x emissions, the well-known P3-T3 method [29] was implemented, whereas for nvPM the approach was largely adapted from the method given by Durdina et al. (2017) [23]. In both methods, the EI is first calculated at a reference condition (in this study, the rated thrust setting under the SLS conditions), and then combustor inlet pressure (P_{t3}) and Fuel-to-Air ratio (FAR) corrections are applied to estimate the EI for a different operating condition (in this study, the cruise condition). Separately, in-house NO_x and nvPM models, for the rich-burn and lean-burn combustion technologies, were developed to estimate the emissions at design conditions for the different engine configurations. These are subsequently described in more detail.

2.3.1. Rich-Burn Combustor Emission Modeling

This section describes the NO_x and nvPM emission models for the rich-burn RQL combustor.

Rich-Burn EINO_x Model

For the cruise EINO_x ($EINO_{x,cruise}$), the P₃–T₃ correlation is shown in Equation (5):

$$EINO_{x,cruise} = EINO_{x,SLS} \cdot \left(\frac{P_{t3,cruise}}{P_{t3,SLS}} \right)^n \cdot \left(\frac{FAR_{cruise}}{FAR_{SLS}} \right)^m \cdot \exp(h) \quad (5)$$

where the EINO_x at the rated thrust, and under SLS conditions ($EINO_{x,SLS}$), is corrected due to the changes in P_{t3} , FAR and atmospheric humidity (h) at cruise conditions to obtain the $EINO_{x,cruise}$, with the same operating combustor inlet temperature (T_{t3}). n and m are the exponents of the pressure and FAR terms, respectively. To estimate the $EINO_{x,SLS}$, the emission correlation was developed as a function of P_{t3} , T_{t3} and FAR, as shown in Equation (6):

$$EINO_{x,SLS} = a \cdot P_{t3}^b \cdot \exp(c \cdot T_{t3}) \cdot d^{(f \cdot FAR)} \quad (6)$$

The ICAO LTO cycle data for three CFM56 models, simulated in GSP, were curved-fitted to obtain the constants in the model, as shown in Equation (7).

$$EINO_{x,SLS} = 0.1921 \cdot P_{t3}^{-0.7686} \cdot \exp(0.0084 \cdot T_{t3}) \cdot 2.01^{(60 \cdot FAR)} \quad (7)$$

This model was tested with two other CFM56 models (eight LTO cycle points) from the ICAO databank and was found to predict the $EINO_x$ within $\pm 10\%$ of the ICAO values, as shown in Figure 4.

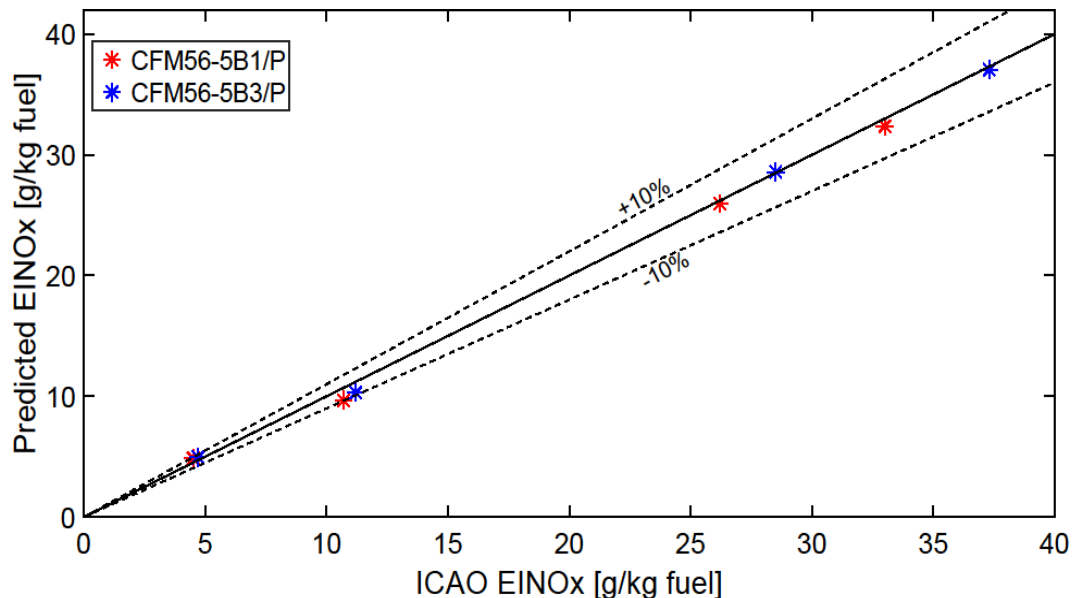


Figure 4. Comparison of the model–predicted $EINO_x$ (Equation (7)) with the ICAO–provided $EINO_x$ under SLS conditions for two CFM56 models (total eight points) for the rich–burn combustor. The solid dashed line is used as a reference to measure the accuracy of the model, with the dashed lines representing a $\pm 10\%$ deviation.

The values of n and m were taken to be 0.3 and 0, respectively, as suggested in the literature for a rich-burn combustion chamber [29]. The humidity correction was found to be approximately 1.13, taken from the ICAO Annex 16 for 60% relative humidity [29] (<https://store.icao.int/en/annexes/annex-16> (accessed on July 2023)).

Rich-Burn nvPM Model

To estimate the nvPM particle number emissions during cruising, first the nvPM mass EI, $EI_{mass,cruise}$, was calculated, using the correlation from Döpelheuer and Lecht (1999) [35], as shown in Equation (8):

$$EI_{mass,cruise} = EI_{mass,SLS} \cdot \left(\frac{P_{t3,cruise}}{P_{t3,SLS}} \right)^{1.35} \cdot \left(\frac{FAR_{cruise}}{FAR_{SLS}} \right)^{2.5} \quad (8)$$

where $EI_{mass,SLS}$ is the nvPM mass EI under rated thrust–SLS conditions. The number emission index at cruise, $EI_{num,cruise}$, can be calculated using a parameter ν , which is the ratio of $EI_{num,cruise}$ to $EI_{m,cruise}$, as shown in Equation (9). ν is a function of T_{t3} and is independent of changes in the altitude [23].

$$EI_{num,cruise} = \nu \cdot EI_{mass,cruise} \quad (9)$$

The $EI_{mass,SLS}$ and ν were modeled as a function of T_{t3} by curve-fitting nvPM data for six different CFM56 engines from the ICAO databank. These include corrections for system losses during measurements, as provided by the databank. $EI_{mass,SLS}$ was fitted with sixth-order polynomials, whereas ν was modeled as a decreasing exponential function of T_{t3} . These are shown in Equations (10)–(12), respectively.

$$EI_{mass,SLS} = (2.798 \cdot t^6) + (0.4 \cdot t^5) - (11.817 \cdot t^4) + (6.313 \cdot t^3) + (38.427 \cdot t^2) + (26.505 \cdot t) + 6.396 \quad (10)$$

$$v = (0.7944e + 14) \cdot \exp(-0.5956 \cdot t) \quad (11)$$

$$t = \frac{T_{t3} - 648.1}{139.2} \quad (12)$$

The $EI_{mass,SLS}$ correlation was tested with LTO cycle data for two other CFM56 engine models (eight LTO cycle points) from the ICAO databank and the model prediction was found to be within $\pm 5\%$ of the ICAO values for the take-off and climb-out thrust settings, as shown in Figure 5. For the lower thrust settings (approach and idle), the correlation became less accurate. As this correlation was to be typically used for cruise T_{t3} values that correspond to thrust settings closer to the climb-out point, it was considered sufficiently accurate for this research.

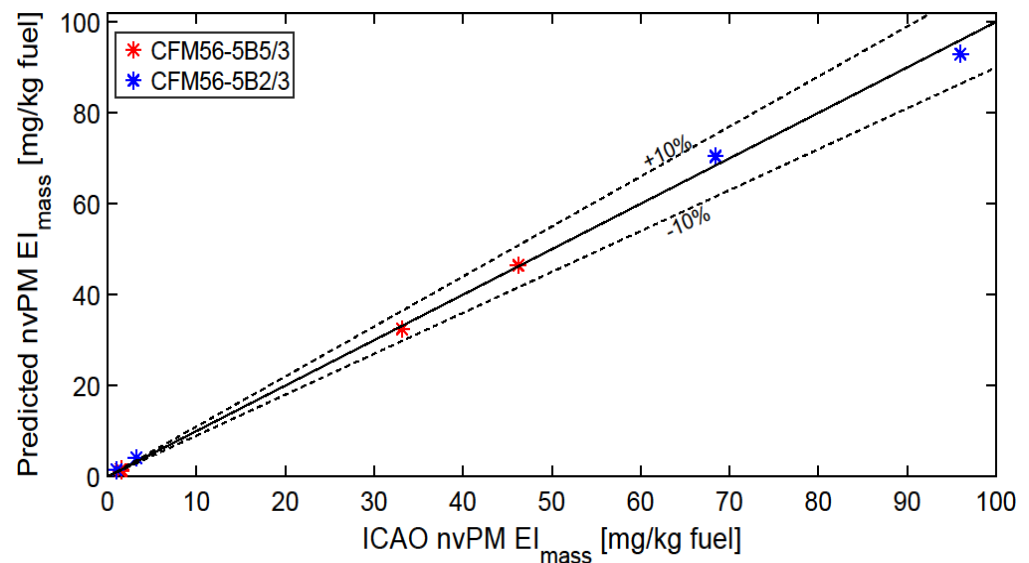


Figure 5. Comparison of the model–predicted $nvPM EI_{mass,SLS}$ (Equation (10)) with ICAO–provided $nvPM$ under SLS conditions for two CFM56 models (total eight points) for the rich–burn combustor. The solid dashed line is used as a reference to measure the accuracy of the model, with the dashed lines representing a $\pm 10\%$ deviation.

Further, to test the validity of the model during cruise, it was applied to a test case given by Durdina et al. (2017) [23] for a Boeing 737NG equipped with a CFM56-7B at cruise. The engine was modeled in GSP, and the given cruise conditions were simulated to obtain the T_{t3} for the subsequent calculation of $nvPM EI$ s. It was found that the $nvPM EI_{mass,cruise}$ was predicted within $\pm 10\%$, and $nvPM EI_{num,cruise}$ within $\pm 6\%$ using the model.

2.3.2. Lean-Burn TAPS-II Emissions Modeling

The TAPS combustion technology implemented in the next-generation LEAP-X engine has a lower $EINO_x$ due to its lean-burn operation. Foust et al. (2012) [36] described the development of the TAPS combustor and gave a comparison of the broad NO_x emission trends of the TAPS combustor with those of the RQL combustor during typical aircraft operating points. For each fuel injector in a TAPS combustor, there is a pilot injector and a concentric outer main injector. The pilot has a rich-burn configuration, which is operational during low-power settings. At high power settings, the fuel is split between the pilot and the main, with most of the fuel injection through the main. The main injection is a set of radial jets that enter a larger air swirler, with a large effective area leading to a leaner fuel burn. The resultant lean combustion leads to lower NO_x emissions. In this research, the NO_x emissions for the TAPS combustor are modeled based on the trends given in [36]. As the thrust value for achieving such reduction has not been explicitly mentioned in the

public domain, in this research, it was assumed that the main burner begins to operate at 40% of the rated thrust for the engine.

Lean-Burn TAPS-II $EINO_x$ Model

Two separate correlations were developed for the pilot and pilot + main operations. ICAO LTO cycle data for six different LEAP engines were considered; that is, twelve LTO cycle data points in each operating regime. The format for these correlations is the same as that in Equation (6), and the model is shown in Equation (13).

$$\begin{aligned} EINO_{x,SLS}^p &= 0.0069 \cdot P_{t3}^{-2.7496} \cdot \exp(0.0216 \cdot T_{t3}) \cdot 9.773^{(13.3701 \cdot FAR)} & F_{engine} \leq 40\% \\ EINO_{x,SLS}^{p+m} &= (3.9072 \cdot 10^{-6}) \cdot P_{t3}^{-13.9974} \cdot \exp(0.0776 \cdot T_{t3}) \cdot 1.4697^{(86.8456 \cdot FAR)} & F_{engine} > 40\% \end{aligned} \quad (13)$$

The above model was tested with LTO cycle data for three other LEAP engines (six data points for each correlation), and the accuracy of the prediction is shown in Figure 6. Specifically, the correlation for pilot operation showed greater accuracy. For the pilot + main operation, the prediction showed a slightly larger deviation. It is expected that as data for more LEAP engine models are provided in the ICAO databank in the future, the correlations could be remodeled, and more accurate predictions could likely be obtained.

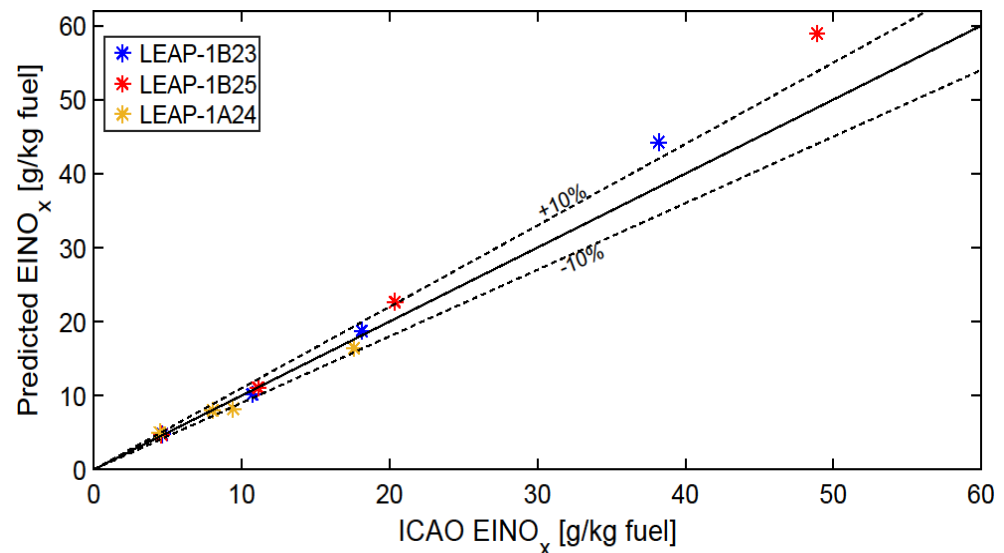


Figure 6. Comparison of the model–predicted $EINO_x$ (Equation (13)) with the ICAO–provided $EINO_x$ under SLS conditions for three LEAP models (total twelve points) for the TAPS–II combustor. The solid dashed line is used as a reference to measure the accuracy of the model, with the dashed lines representing a $\pm 10\%$ deviation.

The $EINO_{x,SLS}$ calculated from the above model was then corrected for changes in altitude and humidity to obtain $EINO_{x,cruise}$ using Equation (5), similar to the rich-burn correlations. The value of n was taken to be 0.2 [29]. m was obtained as -1.1598 from the curve-fitting results derived from A320neo simulations in PIANO-X in cruise mode under standard operating conditions, keeping n fixed. At three different cruise altitudes during the mission, the $EINO_{x,cruise}$ was obtained from PIANO, and the $EINO_{x,SLS}$ was calculated using Equation (13). The details of the simulation are given in the Appendix A.2.

Lean-Burn TAPS nvPM Model

For TAPS nvPM calculations, a similar approach as that used in the $EINO_x$ correlation was applied, with the pilot and pilot + main operation regimes treated separately. Based on the limited data available for the LEAP engines in the ICAO databank, three LEAP engine models were used for obtaining the $EI_{mass,SLS}$ and the ν correlations, and one engine model was used for validation. These include corrections for system losses during measurements,

as provided by the databank. For both operating regimes, exponential functions were implemented. The correlations are shown in Equations (14)–(16), respectively.

$$\begin{aligned} EI_{mass,SLS}^p &= 0.0290 \cdot \exp(4.8961 \cdot t_1) + 0.9562 \cdot \exp(0.2439 \cdot t_1) \quad F_{engine} \leq 40\% \\ EI_{mass,SLS}^{p+m} &= 0.0962 \cdot \exp(2.2046 \cdot t_2) + 1.4302 \cdot \exp(0.2152 \cdot t_2) \quad F_{engine} > 40\% \end{aligned} \quad (14)$$

$$\begin{aligned} \nu^p &= (7.316e + 13) \cdot \exp(0.68 \cdot t_1) \quad F_{engine} \leq 40\% \\ \nu^{p+m} &= (7.61e + 10) \cdot \exp(-0.1061 \cdot t_2) \quad F_{engine} > 40\% \end{aligned} \quad (15)$$

$$\begin{aligned} t_1 &= \frac{T_{I3} - 565.4}{100} \\ t_2 &= \frac{T_{I3} - 817.1}{32.68} \end{aligned} \quad (16)$$

Further, Equation (8) was used for calculating the cruise nvPM emissions, due to a lack of experimental and/or simulation data on offer to determine the exponents of the correction terms for a lean-burn combustor. Figure 7 shows the derived exponential curves, for both the operating regimes, along with the model prediction compared to the known ICAO data. When more data for other LEAP-X models are provided in the future in the ICAO databank, the correlations are expected to provide more accurate results, along with more points to validate them.

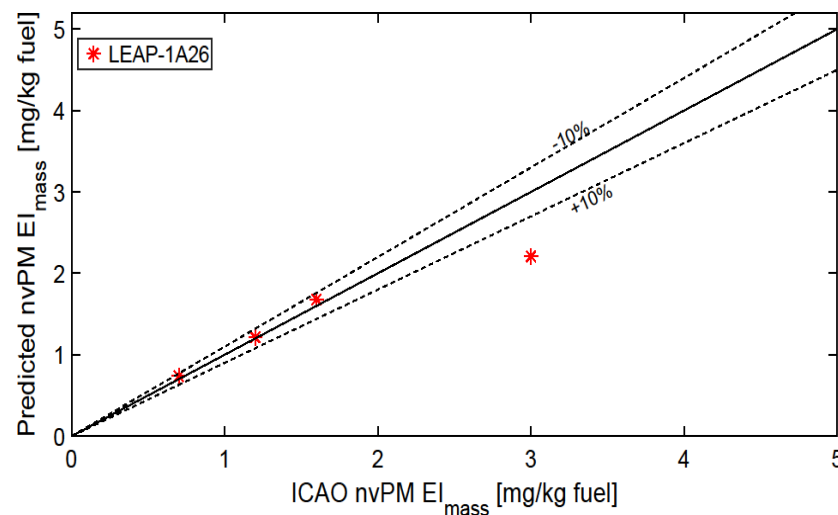


Figure 7. Comparison of the model–predicted nvPM $EI_{mass,SLS}$ (Equation (14)) with ICAO–provided nvPM under SLS conditions for one LEAP–X model (total four points) for the TAPS–II combustor. The solid dashed line is used as a reference to measure the accuracy of the model, with the dashed lines representing a $\pm 10\%$ deviation.

2.4. The Emission Inventory

An emission inventory is a 3D emission data set, containing, as a minimum, annual information about the fuel consumption, the flown distance and NO_x emissions at a certain location in the atmosphere, which are described by the latitude, the longitude, and the pressure altitude, representing a specific atmospheric volume. The city pairs that form the emission inventory are shown in Figure 8, with an equal number of A320 flights in both regions. The geographical distribution of these flights is also shown. For these flights, the data from the OpenSky Network were generated with a time step of 30 s. For each city pair, first, the total great-circle distance was estimated. Then, each step of the modeling chain, as shown in Figure 2, was implemented, which gave the fuel consumption, the NO_x and the nvPM emissions. For each city pair, one flight per day for one year was considered. Thus, the fleet consisted of 60 identical A320 aircraft, with the annual number of flights being 21,900. These data were then converted into a readable format that AirClim used as the emission inventory.

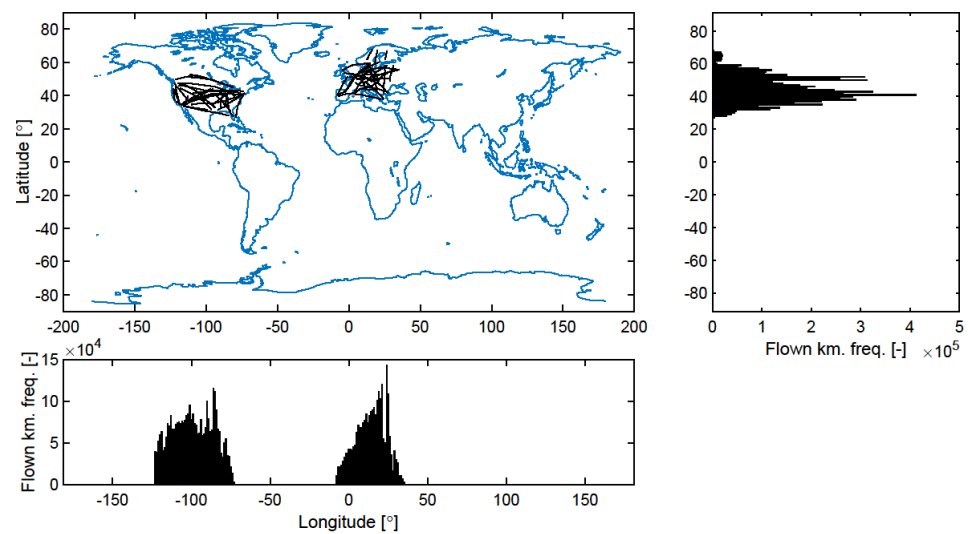


Figure 8. Flight planning consisting of the 60 city pairs. The annual global flown distance frequency distribution is also shown. The lines in the map indicate the flight routing between city pairs across North America and Europe. The bottom panel shows the flight frequency distribution along the longitudinal direction and the figure on the right panel shows the latitudinal distribution of the flight frequency.

2.5. Climate Assessment Model

After the creation of the emission inventory, the background modeling inputs in AirClim were determined. Some information about the past and (expected) future aviation fuel consumption, atmospheric chemical composition, and pre-calculated atmospheric input data obtained from sophisticated climate-chemistry models serve as further inputs into AirClim. AirClim is a non-linear response model, developed based on a detailed atmospheric chemistry process based on simulation results from a climate chemistry model (CCM), used to evaluate the climate impact of given aircraft engine technologies considering different scenarios. Non-CO₂ effects are complex as they have strong spatial and temporal resolutions. AirClim balances the level of details and the model fidelity, hence is a good candidate to evaluate aviation's climate impact. There are several climate metrics, e.g., the widely used global warming potential (GWP). The selection of the metric depends on the specific question to be answered. Megill (2023) [37] analyzed different metrics based on six criteria, and indicated that average temperature response (ATR) is the proper metric considering the stability and the direct indication of the global warming effect, and is a suitable metric as far as the comparison of aviation technology is concerned. Furthermore, the time horizon of 100 years balances the long-term and short-term effects.

Essentially, the aviation fuel consumption scenario and the atmospheric CO₂ and CH₄ concentration scenarios serve as the main background modeling inputs in AirClim. In this research, the CurTec scenario taken from Grewe et al. (2021) [15] was considered as the aviation fuel consumption scenario. Figure 9 shows the trend for the same. The scenario is described up to 2100 in the original file, whereas the trend beyond 2100 (dashed line) is assumed to be based on the annual fuel change rate in the year 2100.

For the atmospheric CO₂ and CH₄ concentration scenarios, the IPCC SSP2-4.5 scenario is considered [38]. This is the so-called “Middle of the Road” scenario, where the pace of sustainable development is relatively slow, and global resource and energy usage rates decline. Figure 10 shows the trends of the atmospheric concentration of the two species.

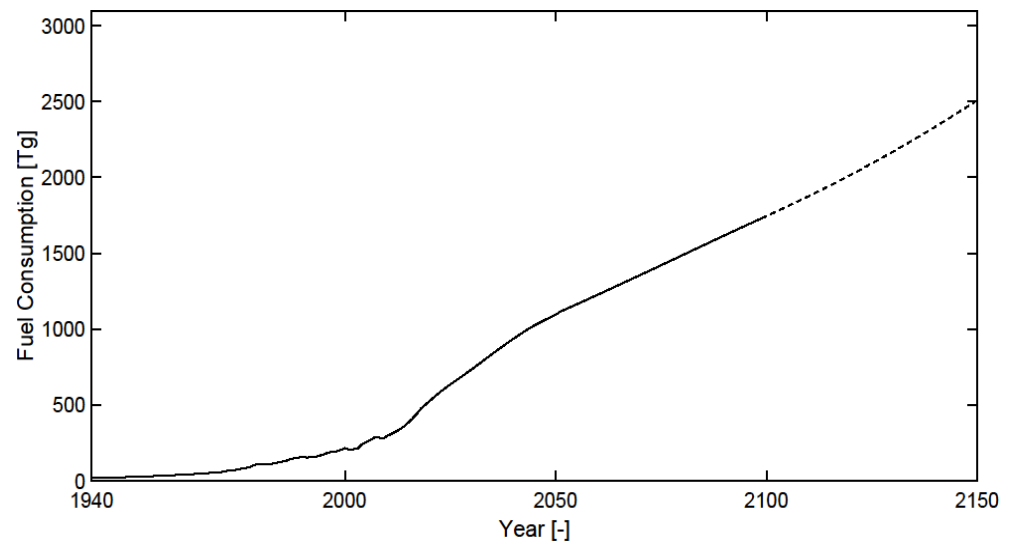


Figure 9. CurTec aviation fuel scenario [15]. The dashed-line-indicated trend beyond 2100 assumes that the annual fuel change remains the same as in 2100.

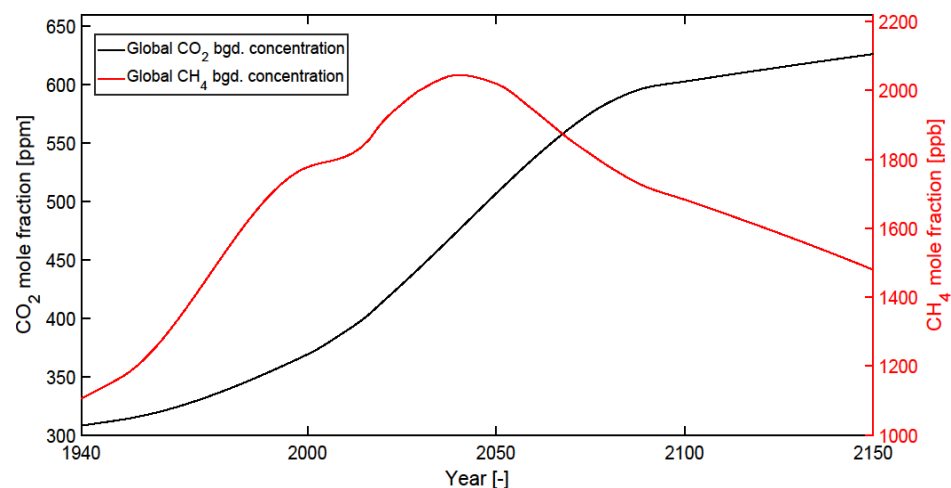


Figure 10. Background atmospheric CO₂ (in black) and CH₄ (in red) concentration trends for the IPCC SSP2-4.5 scenario [38]. The units for the CO₂ trends are in parts-per-million (ppm), whereas for the CH₄ they are in parts-per-billion (ppb).

The complete methodology was repeated for each change in the OPR and TIT of the baseline engine. The OPR was varied from 25 to 40 in steps of 5. The TIT was varied from 1450 K to 1800 K. At the lower end of the TIT range, the resolution was kept smaller, at 25 K, to capture the finer trends of fuel consumption and NO_x emissions. For other cases, the resolution was kept at 50 K. Further, the TIT was varied at the baseline OPR, and vice-versa. A total of 55 configurations were modeled in addition to the baseline engine. For each configuration, the cruise nvPM particle number emissions of the fleet were estimated using the nvPM emission model. Accordingly, the changes in contrail-induced RF ($RF_{contr.}$), i.e., $\Delta RF^{contr.}$ were estimated relative to the baseline configuration using the correlation given in Grewe et al. (2021) [15], shown in Equation (17), where Δpn is the relative change in particle number emissions of nvPM. It is to be noted that the correlation is only valid for $\Delta pn \geq 0.1$. This factor was then used in AirClim to determine the impact on the $RF_{contr.}$ and its subsequent temperature change ($\Delta T_{s,contr.}$).

$$\Delta RF^{contr.} = \frac{\arctan(1.9\Delta pn^{0.74})}{\arctan(1.9)} \quad (17)$$

The climate simulations start in 2015 and end in 2150. The ATR_{100} is measured from the year 2035, the year when technological options are representative. Thus, this is the year corresponding to which the background scenario is scaled according to the total fuel consumption from the various emission inventories. Essentially, the emission inventory represents the global distribution of emissions and flow distances for this year, and the temporal development of these is represented by the CurTec scenario shown in Figure 9.

2.6. Modelling Uncertainties

Since the analysis is highly multi-disciplinary in nature, there are uncertainties that can arise due to uncertainties within different sub-models. Regarding flight profiles, we consider only 60 city pairs with A320 being operational, which is a small subset of global aviation. One source of uncertainty is the factors/variables that have been taken to be constant but can change in practice, e.g., the payload. Another source of uncertainty in the modeling chain is the NO_x and nvPM emission models. Even though the emissions have been validated using the four ICAO engine test points, the behavior of emissions between these points is interpolated. This may lead to some uncertainties in the emission predictions. In addition, the emissions are also affected due to changes in operating conditions, such as cruise altitude (considered fixed in this research), the engine power levels, and atmospheric humidity change. Kroon (2022) [39] analyzed the uncertainty of the NO_x emission index subject to different sources, e.g., engine aging, which will be applied to the current research for uncertainty analysis. Regarding the climate model, using a different climate chemistry model or cloud scheme in AirClim (within the precalculated atmospheric input data [5,28]) may lead to deviations in the ATR_{100} . In addition, there are uncertainties related to the lifetime, climate sensitivity parameter and RF for the emission species [5,28].

3. Results and Discussion

This section discusses the results of the research. The key results that are discussed are the variations in fuel consumption, NO_x emissions, nvPM particle number and the climate response in ATR_{100} . Together, they are called the resultant parameters in this research.

The results are presented in two parts. First, the values of the resultant parameters are discussed for the baseline engine (Section 3.1). They serve as the reference for the results of other engine configurations, which are presented next (Section 3.2). These are in the form of contour plots against the variation of the OPR (X-axis) and the TIT (Y-axis). The values of the resultant parameters are normalized with respect to the corresponding values for the baseline engine configuration. Further, the configurations with minimum fuel burn at each OPR are taken, and a comparison of the temporal development of various species' responses as well as of the ATR_{100} is made.

3.1. Resultant Parameters for the Baseline Engine Configuration

Table 1 shows the resultant parameters for the baseline configuration. These represent the results at the fleet level, i.e., the resultant parameters across the 60 city pairs. The mean $EINO_x$ and nvPM $EI_{num.}$ are also shown. The nvPM particle number serves as the reference against which particle numbers for other configurations are compared, and Equation (17) is applied to estimate the $RF_{contr.}$ reduction. The ATR_{100} measured from 2035 up to 2134 is 0.085 mK. This is the sum of the response of the six principal species calculated in AirClim: CO_2 , H_2O , contrails, NO_x -induced O_3 enhancement, NO_x -induced CH_4 depletion and the subsequent PMO effects.

Table 1. Resultant parameters for the baseline CFM56. Fuel consumption and emissions are based on 60 city pairs.

Config.	Fuel Consumption	NO _x Emissions	Mean EI _{NO_x}	nvPM No. ($\times 10^{20}$)	Mean EI _{num.} ($\times 10^{14}$)	ATR ₁₀₀
	(t(Fuel))	(t(NO ₂))	(g(NO ₂)/kg Fuel)	(#(nvPM))	(#(nvPM)/kg Fuel)	(mK)
Baseline (A320 and CFM56)	279.28	3.11	11.1	1.40	5.01	0.085

3.2. Parametric Results

3.2.1. Rich Burn Combustor Configurations

Variation in Fuel Consumption

Figure 11 shows the cruise fuel consumption trend normalized to the baseline configuration value. While fuel consumption reduces with increasing OPR, the dependency on TIT is not straightforward. For very low TITs (e.g., TIT = 1450 K), the engine specific thrust reduces, leading to a relatively larger core and increased fuel consumption with respect to baseline. Conversely, for very high TITs (e.g., TIT = 1800 K), there are more core nozzle losses, which again leads to higher fuel consumption with respect to baseline. This distinction becomes more prominent at higher OPRs. Hence, at every OPR, a TIT exists at which the fuel consumption is the lowest, and this TIT is higher for a higher OPR.

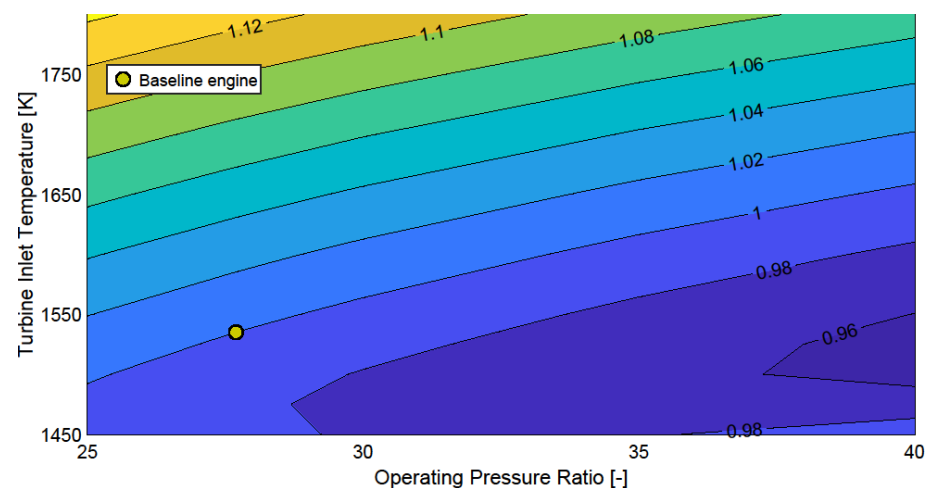


Figure 11. Cruise fuel consumption of the fleet with varying OPR and TIT for the rich-burn combustor configurations, normalized to the baseline (yellow circle), which is 279.28 t(fuel) (Table 1).

Variation of Emissions

Figure 12 shows the cruise NO_x trend, normalized with the corresponding baseline engine NO_x (3.11 t(NO₂)). Aviation NO_x production is mainly influenced by the pressure and temperature during combustion, which increases with OPR. Similarly, a higher TIT implies that the temperature in the combustor is still high, leading to higher NO_x emissions with respect to baseline. Compared to Figure 11, it is observed that the respective reduction and increase in fuel consumption and NO_x with changing design parameters are not similar. While fuel consumption typically reduces by less than 10% with increasing OPR, NO_x can increase by 30 to 50%, depending on the TIT at which these trends are observed.

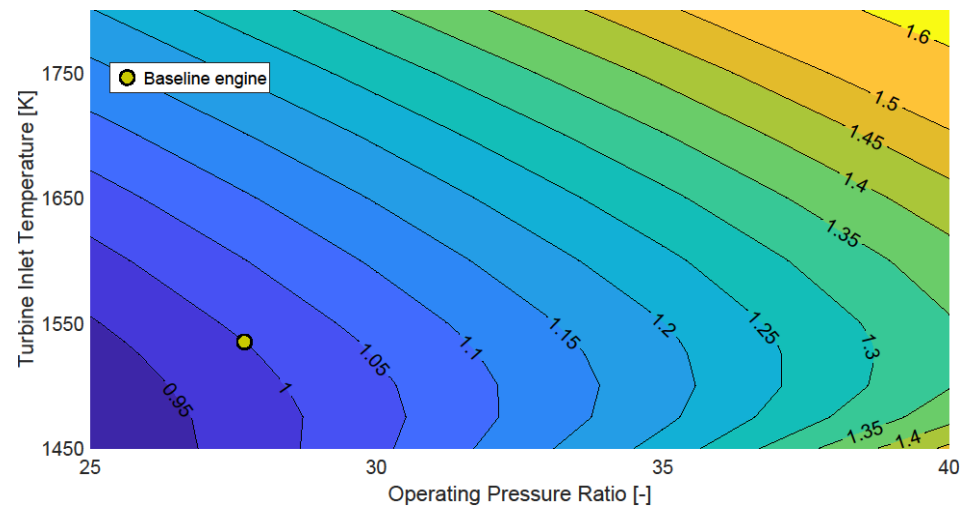


Figure 12. Cruise NO_x emissions of the fleet with varying OPR and TIT for the rich-burn combustor configurations, normalized to the baseline (yellow circle), which is 3.11 t(NO_2) (Table 1).

The trend for the nvPM particles is shown in Figure 13. As the combustor inlet pressure and temperature increase with OPR, it makes conditions favorable for nvPM formation [40,41]. A high degree of non-linearity in nvPM formation with respect to increasing OPR is observed, with nvPM formation rapidly rising to be close to (and even greater at higher TITs) three times the baseline value at OPR = 40. In addition, an increasing TIT leads to greater nvPM formation due to the increased temperatures and fuel/air ratio within the combustor. At low OPRs (e.g., OPR = 25 and 30), nvPM formation exhibits mild sensitivity to TIT changes, and vice versa. Overall, the non-linear behavior of nvPM formation is mainly influenced by the formation of radical precursors (Warnatz et al., 2012) and changes in fuel consumption with design parameters, along with some degree of particle coagulation at high temperatures [23].

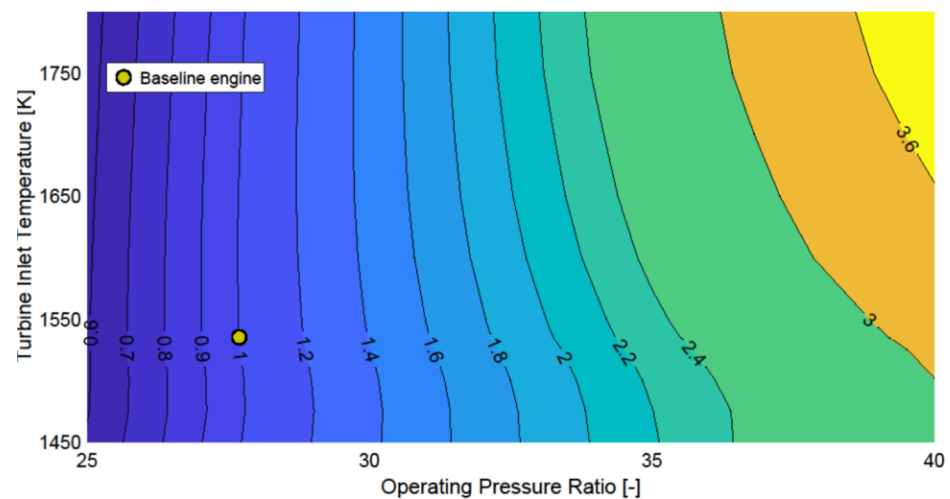


Figure 13. Cruise nvPM number of the fleet with varying OPR and TIT for the rich-burn combustor configurations, normalized to the baseline (yellow circle), which is 1.4×10^{20} (#nvPM) (Table 1).

Variation of ATR_{100}

The ATR_{100} trend for the rich-burn combustor is shown in Figure 14. The ATR_{100} increases with OPR, with the trend being similar to the non- CO_2 emission trends shown in Figures 12 and 13. At low OPRs (e.g., OPR = 25 and 30), the increase in the TIT leads to smaller changes in the ATR_{100} . As the OPR increases, the sensitivity of the ATR_{100} with respect to TIT also increases, as smaller increments in the TIT lead to large ATR_{100} changes.

This effect is more pronounced at high OPR and TIT configurations—see the top right area of the figure.

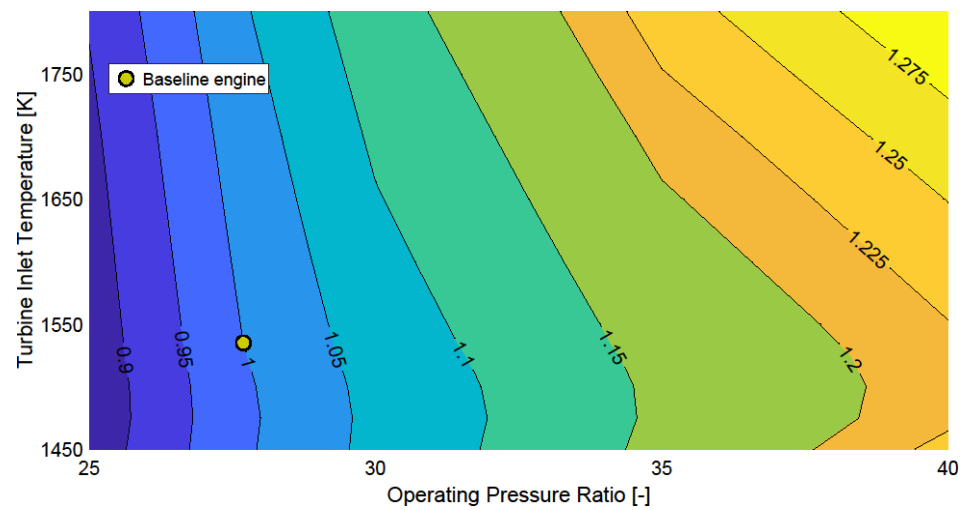


Figure 14. ATR₁₀₀ with varying OPR and TIT for the rich-burn combustor configurations, normalized to the baseline (yellow circle), which is 0.085 mK (Table 1).

3.2.2. Lean-Burn Combustor Configurations

Variation of Emissions

Figure 15 shows the cruise NO_x trend for the TAPS-II configurations. Compared with Figure 12, the emissions' magnitude has reduced drastically, while showing similar trendlines. This reduction is larger at lower OPRs (e.g., OPR = 25 and 30), in the range of 30 to 40%, where low combustor pressure and temperature synergize well with lean combustion. The NO_x emissions increase with the OPR and TIT, and the reduction with respect to the rich-burn configuration is only about 20% for OPR = 40. Further, a degree of non-linearity is also observed, around higher TIT values, indicating that NO_x emissions can change rapidly for the TAPS-II combustor at higher design parameters, in contrast with the trends in Figure 12, where the contour lines are “smoother”, indicating more monotonous trends.

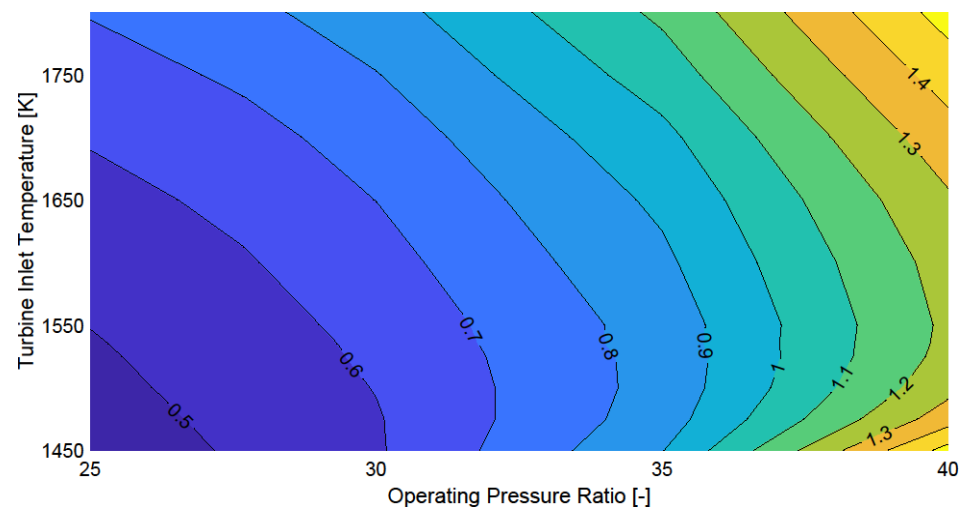


Figure 15. Cruise NO_x emissions of the fleet with varying OPR and TIT for the TAPS-II combustor configurations, normalized to the baseline, which is 3.11 t(NO₂) (Table 1).

The nvPM number trend for the TAPS-II configurations is shown in Figure 16. The TAPS-II combustor reduces the EI_{num,cruise} of nvPM by approximately four orders of

magnitude (1014 for the rich-burn combustor vs. 1010 for the TAPS-II) at cruise. A similar reduction is also observed in the data from the ICAO databank for engines with similar thrust levels. The lean combustion regime of the TAPS-II heavily influences the nvPM production, resulting in a drastic reduction in the particle numbers. The sensitivity of the nvPM number with respect to TIT has also increased, with it being a far more influential factor, especially at lower OPRs. Overall, with increasing OPR and TIT, the nvPM emissions increase, with the total emissions lower compared to the corresponding rich-burn configurations.

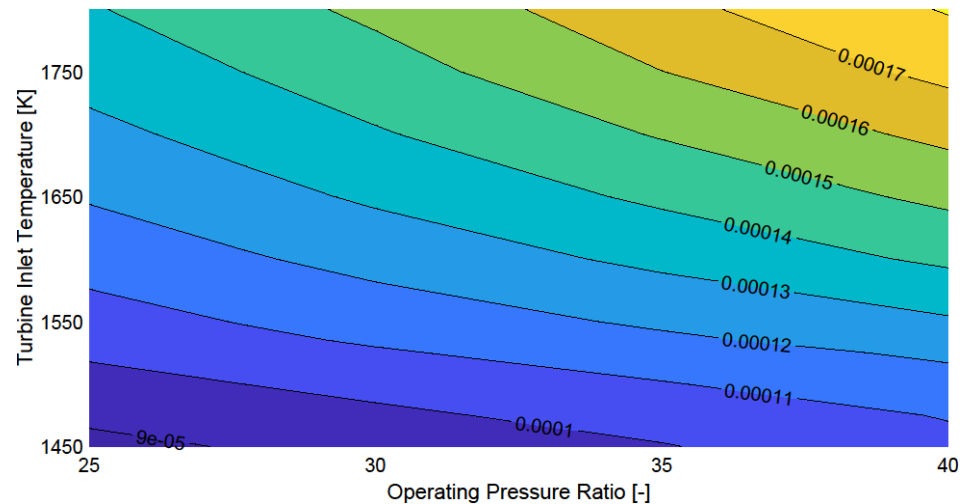


Figure 16. Cruise nvPM number of the fleet with varying OPR and TIT for the TAPS-II combustor configurations, normalized to the baseline, which is 1.4×10^{20} (#nvPM) (Table 1).

Variation of ATR_{100}

The TAPS-II configuration ATR_{100} trend is shown in Figure 17. Relative to the corresponding rich-burn configuration, the ATR_{100} was reduced by approximately 50 to 60% for low OPRs (i.e., OPR = 25 and 30), and close to 70% for the higher OPRs (i.e., OPR = 35 and 40). Furthermore, with the change in the OPR, the change in the ATR_{100} was smaller, only about 10 to 12% from OPR = 25 to 40, compared to the rich-burn trend, where the same can be seen to be closer to 40%. In addition, the trend closely resembles the lean-burn NO_x emission trend, shown in Figure 15.

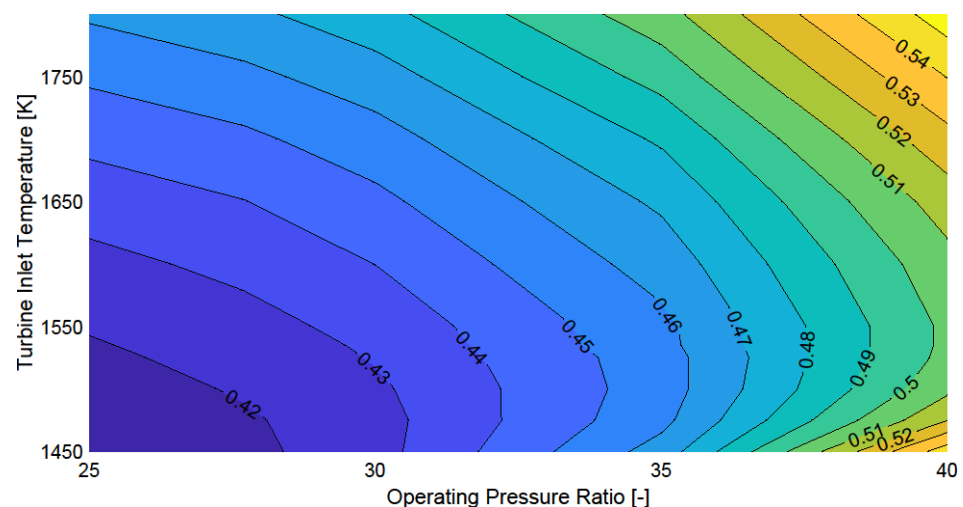


Figure 17. ATR_{100} with varying OPR and TIT for the TAPS-II combustor configurations, normalized to the baseline, which is 0.085 mK (Table 1).

3.3. Climate Impact Analysis for Engines with a Minimal Fuel Burn

Irrespective of the combustion technology, the ATR100 trends are largely aligned with those of the two main non-CO₂ emissions discussed. To analyze the species' impact and their relative contribution, the temporal evolutions of the temperature response of the different species were analyzed. This enables the identification of species most critical for the total climate impact. In addition, the species' contributions to the total ATR₁₀₀ were also investigated, considering configurations with minimum fuel consumption at each OPR. The trend for the temperature response due to the CO₂ emissions is shown in Figure 18. The trends for both combustor technologies are identical, as there is no difference in the fuel consumption modeled between the two technologies. Throughout the simulation, the CO₂ response rose slowly, reaching 0.025 mK for the baseline engine in 2150, relative to 2015. This is a result of the well-mixed nature of CO₂, leading to a larger response time, on the order of decades to centuries. It can also be concluded from Figure 18 that the reduction obtained in the CO₂ response decreased as the OPR increased, with the lines for OPR = 35 and 40 placed closer to each other compared to OPR = 25 and 30.

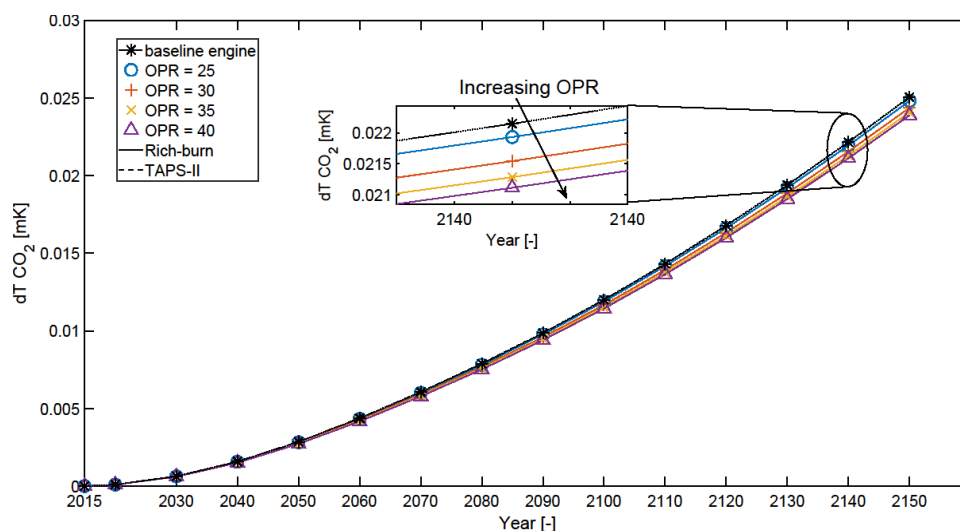


Figure 18. Temporal evolution of the temperature response due to CO₂ emissions (dT_{CO_2}) for baseline engine (dotted-asterisk line) and the OPR range from 25 to 40. The trends are shown for both combustor technologies (in this case, they result in identical trendlines). The response due to the different configurations is also shown for the year 2140.

The trends for the NO_x temperature response are shown in Figure 19. Not only was the NO_x temperature response higher than the CO₂ temperature response, but the deviation from the baseline was also larger, with clear distinctions very early during the simulation. The difference between the two combustor technologies was much larger for lower OPRs, in line with the observations in Figures 12 and 15. It was also observed that the NO_x response for OPRs 30 and 35 for the TAPS-II combustor was still lower than the baseline configuration, which highlights its potential use in reducing the impact of NO_x-related effects in engines operating at higher OPRs.

The contrail trends are shown in Figure 20. Effectively, with increasing OPR, the contrail response increased, due to the increased nvPM acting as a contrail precursor. While the TAPS-II combustor reduced the contrail effects relative to the rich-burn combustor due to the large reduction in nvPM, a threshold exists below which these effects diminished. At very low nvPM numbers, the particles were mixed in and formed droplets, which resulted in an approximately constant, low ice crystal number equaling the cloud condensation nuclei. However, there was some condensation of heavier volatile particles in the exhaust plume, e.g., sulfates, which contribute to contrail formation. This uncertainty in ice crystal

formation is defined by the $\Delta p_n \geq 0.1$ limit in Equation (17), resulting in a constant response for the TAPS-II configurations with changing OPR, at 0.037 mK in 2150 relative to 2015.

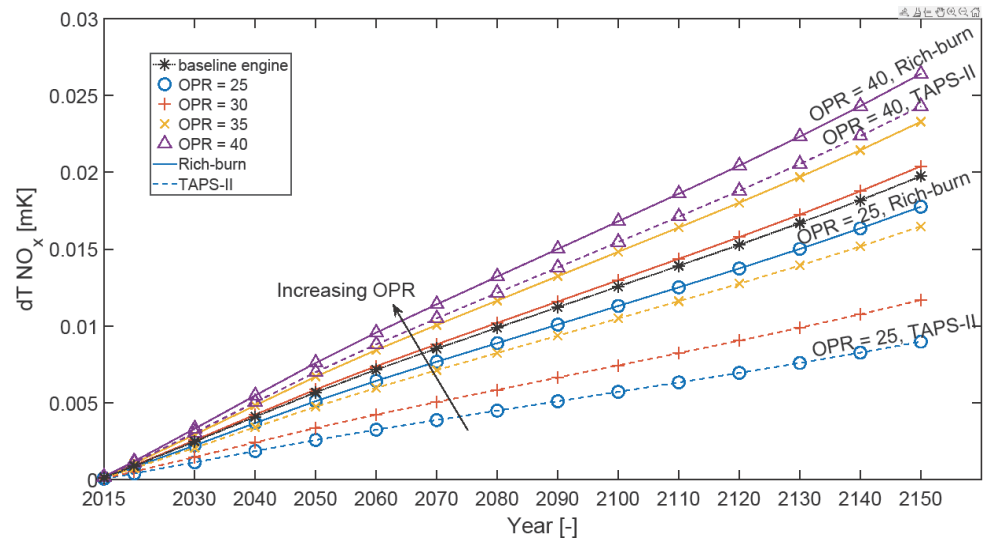


Figure 19. Temporal evolution of the temperature response due to NO_x emissions (enhancement effects due to O₃ production and diminishing effects due to CH₄ and PMO) for baseline engine (dotted asterisk line) and the OPR range from 25 to 40. Solid lines represent rich-burn configurations, whereas dashed lines represent TAPS-II configurations.

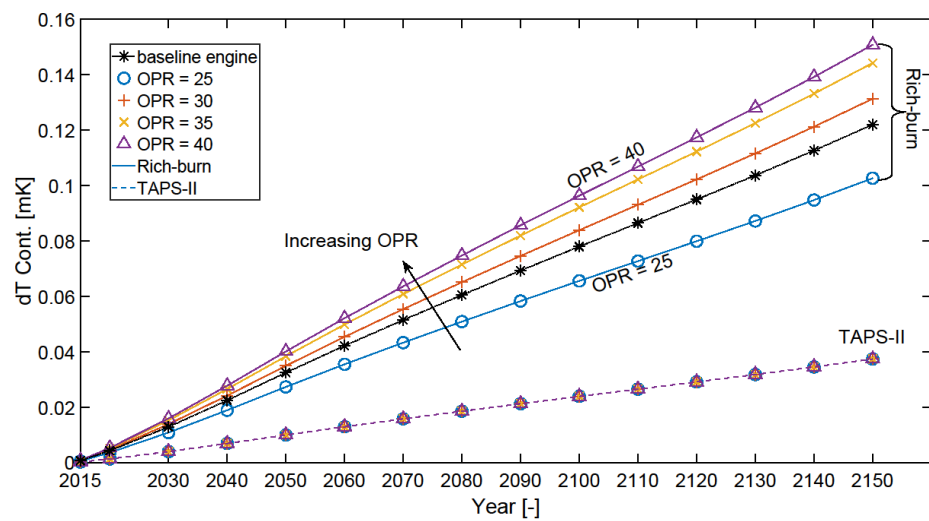


Figure 20. Temporal evolution of the temperature response due to contrail effects (dT Cont.) for baseline engine (dotted asterisk line) and the OPR range from 25 to 40. Solid lines represent rich-burn configurations, whereas dashed lines represent TAPS-II configurations.

The NO_x and contrail responses combined made a large contribution to the total non-CO₂ response, as shown in Figure 21. There was a small contribution of H₂O impact, although this was negligible. The non-CO₂ impact trendline showed a much steeper slope throughout the simulation compared to the CO₂ impact trendline, with the baseline engine configuration reaching up to 0.144 mK, in the year 2150, compared to the reference in 2015. For the TAPS-II combustor, the non-CO₂ response was lower, highlighting the effect of lean combustion on the nvPM formation and NO_x emissions, which subsequently reduced the contrail and NO_x effects.

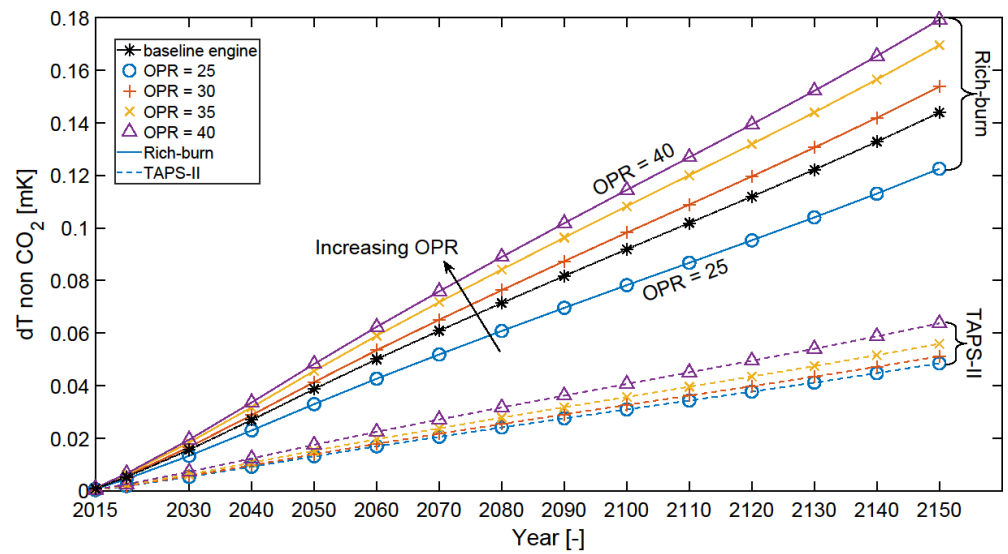


Figure 21. Temporal evolution of the temperature response due to the non-CO₂ emissions (dT NO_x, H₂O, and contrails) for baseline engine (dotted-asterisk line) and the OPR range from 25 to 40. Solid lines represent rich-burn configurations, whereas dashed lines represent TAPS-II configurations.

The total temperature response is shown in Figure 22, largely resembling the non-CO₂ impact trendline, due to the higher contribution and magnitude of these effects. It can be observed that the contrail response contributes the largest to the total climate impact. In 2150, the contribution of the non-CO₂ effects ranges typically from 83 to 88% for the rich-burn combustor and around 65–70% for the TAPS-II combustor, highlighting the difference in the sensitivities of the total response with respect to changing OPR between the rich-burn and TAPS-II combustors. Overall, the TAPS-II combustor shows a favorable performance in terms of climate response compared to the rich-burn combustor with increasing OPRs.

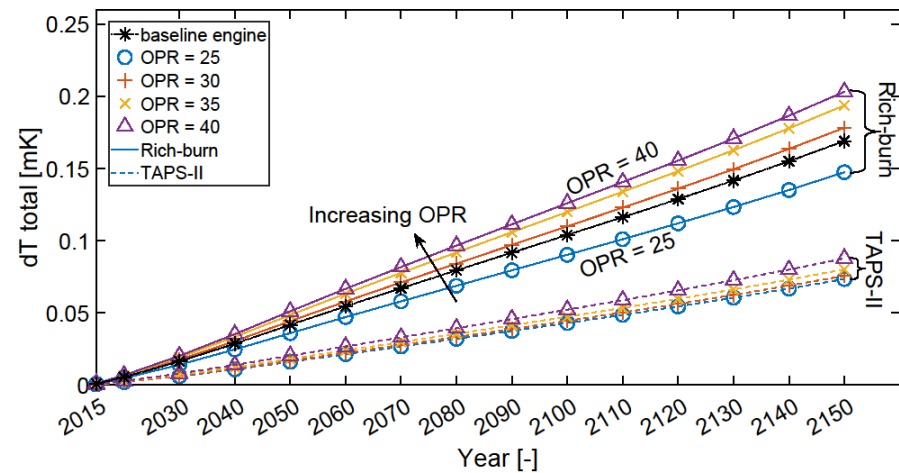


Figure 22. Temporal evolution of the total temperature response for baseline engine (dashed asterisk line) and an OPR ranging from 25 to 40. Solid lines represent rich-burn configurations, whereas dashed lines represent TAPS-II configurations.

To highlight the species’ contributions over the 100-year horizon, Figure 23 shows the ATR100 for these configurations. Comparisons were made for the species with each other, as well as for the two combustor technologies. The total response increased with increasing OPR, corresponding to the trend in Figure 22, for both the rich-burn and TAPS-II configurations. Relative to the rich-burn combustor, the contrail climate impact reduced to the threshold value for the TAPS-II with increasing OPR, and subsequently, the relative

contribution decreased as well, with the contribution of NO_x impact starting to increase. The contribution of the non- CO_2 effects ranged from approximately 85 to 92% for the rich-burn combustor and around 70–80% for the TAPS-II combustor, highlighting the significance of non- CO_2 emissions and their effects.

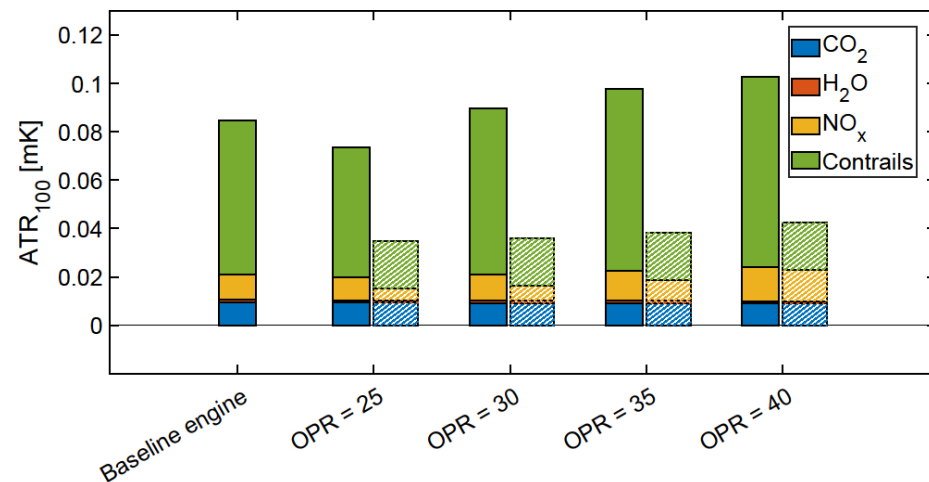


Figure 23. Comparison of the ATR_{100} for each of the six species for the lowest fuel consumption configurations with changing OPR. The trends for the rich burn combustor are shown in solid, whereas those for the TAPS-II combustor are shown as hatched.

To quantitatively analyze the climate sensitivities with respect to engine design parameters, a parameter called the engine design species climate sensitivity has been introduced, which is given in Equation (18):

$$(\gamma_{spec})_h = \left(\frac{\left(\frac{\Delta \text{ATR}_{spec.}}{\text{ATR}_{baseline}} \right)}{\left(\frac{\Delta \text{DesignParam.}}{\text{BaselineParam}} \right)} \right)_h \quad (18)$$

h is the time horizon, i.e., 100 years. This parameter can be used to analyze the total and the individual species' sensitivities with respect to engine design. Some exemplary results are given in Table 2, where the sensitivity of a few key species and the total impact with respect to the changing OPR are shown for the two combustion technologies. Similar sensitivities can be estimated for any range of parameters within the design space.

Table 2. $(\gamma_{spec})_{100}$ values for CO_2 , NO_x , contrails, and total climate impact for two exemplary cases over a time horizon of 100 years for the two combustion technologies.

Design Parameter	Combustor Technology	$(\gamma_{total})_{100}$	$(\gamma_{\text{CO}_2})_{100}$	$(\gamma_{\text{NO}_x})_{100}$	$(\gamma_{\text{Contrails}})_{100}$
OPR (27.69 to 40 at TIT = 1535 K)	Rich burn	0.4964	−0.0989	0.7645	0.5512
OPR (27.69 to 40 at TIT = 1535 K)	TAPS-II	0.4112	−0.0989	2.7404	0

Some interesting insights can be gained from Table 2. The γ_{CO_2} indicates a reduction in the CO_2 response with increasing pressure ratio. $\text{ATR}_{100, \text{NO}_x}$ was the most sensitive to OPR increases, with the TAPS-II configuration showing much higher sensitivity. Further, in this comparison, the γ_{Contrail} and γ_{total} in the rich-burn configuration showed similar magnitudes of change, indicating that contrails are the critical factor in the total climate impact. The $\gamma_{\text{contrails}}$ values did not change in the TAPS-II case, due to the contrail RF reduction threshold.

In this research, we investigated how the engine core design and combustion technology development of a civil turbofan engine has an impact on global temperature change based on a subset of the global flight network for a short-to-medium-range aircraft. The

climate impacts of CO₂, NO_x, H₂O, and contrails were included. The OPR and the TIT were systematically changed within a design space to create a matrix of engine configurations for two different combustion technologies, the rich-burn combustor and the lean-burn TAPS-II combustor. Corresponding to each of these configurations, the ATR₁₀₀ climate metric was calculated and an exhaustive comparison was made. In this research, other aspects of engine integration such as engine weight, size, and installation drag penalties were not considered.

The climate impact of emissions adds a critical dimension as far as engine designs (current and future) are concerned and is currently not included in the engine design stage. In addition, this research also aims to raise general awareness, particularly about non-CO₂ emissions and their climate effects in aviation. The general discourse tends to focus on CO₂ emissions and affinity towards flying; however, non-CO₂ emissions are responsible for a larger contribution towards the climate impact of aviation, as these emissions tend to stay for longer in the atmosphere due to a lack of washout processes. With an increase in passenger traffic as predicted by ICAO, it becomes important that the key issues are focused upon, and policies be formulated in accordance.

4. Conclusions

The results demonstrate that for short-to-medium-range aircraft such as the A320, increasing the engine OPR and TIT will lead to higher NO_x and nvPM emissions. Also, the reduction in CO₂ impact due to reduced fuel consumption is not enough to compensate for such negative effects. With increases in the OPR from 25 to 40, the total ATR₁₀₀ increases by 40%, mainly dominated by the increase in the NO_x and contrails' effects by 49% and 47%, respectively, for rich-burn combustion. The TAPS-II combustor reduces the total ATR₁₀₀ by 52% and 58% for OPR = 25 and 40, respectively. This is due to the contrails' effects being reduced by 63% and 75%, and the NO_x effects being reduced by 49% and 8% for OPR = 25 and OPR = 40, respectively. These results provide novel insights into designing turbofans with the climate impact perspective in consideration, although these are dependent on the chosen flight profiles.

The uncertainties in the results may be due to emission modeling, flight profiles and the climate model implemented. Some of these uncertainties can be reduced to a large extent by using an extensive global flight inventory, a detailed combustion model and integrating Monte-Carlo simulations within the modeling chain.

Author Contributions: Conceptualization, F.Y.; methodology, F.Y. and H.S.S.; validation, H.S.S. and F.Y.; software, H.S.S.; formal analysis, H.S.S.; investigation, H.S.S.; writing—original draft preparation, F.Y. and H.S.S.; writing—review and editing, F.Y., A.G.R., V.G. and H.S.S.; supervision, F.Y., A.G.R. and V.G.; funding acquisition, F.Y. All authors have read and agreed to the published version of the manuscript.

Funding: This research was funded by the Dutch Research Council (NWO) with the grant number 17367 and the Horizon Europe with the grant number 101056863.

Data Availability Statement: The dataset produced in this study is available on the 4TU.ResearchData repository with the DOI: 10.4121/edf74400-173c-4efb-9c68-43ee1a090bdd.

Conflicts of Interest: The authors declare no conflict of interest.

Abbreviations

ACARE	Advisory Council for Aviation Research and Innovation in Europe
ATR	Average Temperature Response
BPR	Bypass Ratio
CCM	Climate Chemistry Model
CORSIA	Carbon Offsetting and Reduction Scheme for International Aviation
EI	Emission Index

ERF	Effective Radiative Forcing
FAR	Fuel-to-Air ratio
GSP	Gas Turbine Simulation Program
GWP	Global Warming Potential
ICAO	International Civil Aviation Organization
LB	Lean Burn
LEAP	Leading Edge Aviation Propulsion
LTO	Landing and Take-off Cycle
nvPM	Non-volatile Particulate Matter
OEW	Operating Empty Weight
OPR	Operating Pressure Ratio
PMO	Primary-mode Ozone
RF	Radiative Forcing
RQL	Rich-Burn Quick-Quench Lean-burn
SLS	Static Sea-Level
TAPS	Twin Annular Premixed Swirler
TIT	Turbine Inlet Temperature
TSFC	Thrust-Specific Fuel Consumption
Symbols	
ATR_{100}	Average Temperature Response over 100 years
$ATR_{baseline}$	ATR for the baseline configuration
BaselineParam.	Baseline Engine Design Parameter
d_{cruise}	Cruise Distance
$EI_{mass,cruise}$	nvPM Cruise Mass Emission Index
$EI_{mass,SLS}$	nvPM SLS Mass Emission Index
$EI_{mass,SLS}^p$	nvPM SLS Mass Emission Index for <i>pilot</i> Operation
$EI_{mass,SLS}^{p+m}$	nvPM SLS Mass Emission Index for <i>pilot + main</i> Operation
$EINO_{x,cruise}$	Cruise NO _x Emission Index
$EINO_{x,SLS}$	SLS NO _x Emission Index
$EINO_{x,SLS}^p$	SLS NO _x Emission Index for <i>pilot</i> Operation
$EINO_{x,SLS}^{p+m}$	SLS NO _x Emission Index for <i>pilot + main</i> Operation
$EI_{num,cruise}$	nvPM Cruise Number Emission Index
$EI_{species}$	Species Emission Index
FAR_{cruise}	Cruise FAR
FAR_{SLS}	SLS FAR
$F_{avg.aircraft}$	Average Aircraft Cruise Thrust
$F_{avg.engine}$	Average Engine Cruise Thrust
F_{engine}	Engine Thrust Level
$(\gamma_{spec.})_h$	Engine Design Species Climate Sensitivity over a Time Horizon of <i>h</i> Years
h	Atmospheric Humidity
h_{cruise}	Cruise Altitude
L/D	Lift-to-Drag Ratio
m	FAR-Term Exponent in P3–T3 Correlation
n	Pressure-Term Exponent in P3–T3 Correlation
P_{t3}	Combustor Inlet Pressure
$P_{t3,cruise}$	Cruise Combustor Inlet Pressure
$P_{t3,SLS}$	SLS Combustor Inlet Pressure
$RF_{contr.}$	Contrail Radiative Forcing
t_{cruise}	Cruise Time
T_{t3}	Combustor Inlet Temperature
\dot{w}_a	Intake Air Mass Flow Rate
$W_{app.payload}$	Apparent Payload Weight
W_{end}	Aircraft Weight at the End of Cruise
$W_{f,cruise}$	Cruise Fuel Weight
$\dot{w}_{f,cruise}$	Cruise Fuel Flow Rate
WNO _x	NO _x Emission Weight

$W_{species,cruise}$	Weight of Emission Species
W_{start}	Aircraft Weight at the Beginning of Cruise
$\Delta ATR_{spec.}$	Change in Species ATR
$\Delta DesignParam.$	Change in Engine Design Parameter
Δpn	Relative Change in nvPM Number Emissions
ΔRF^{contr}	Change in Contrail Radiative Forcing
$\Delta T_{s,contr}$	Temperature Change due to Contrail-Induced Radiative Forcing
ν	nvPM Number-to-Mass Emission Index Ratio
ν^P	nvPM Number-to-Mass Emission Index Ratio for <i>pilot</i> Operation
ν^{p+m}	nvPM Number-to-Mass Emission Index Ratio for <i>pilot + main</i> Operation

Appendix A

Appendix A.1. Validation Cases of the Aircraft Performance Model

This section provides the details of the validation cases for the aircraft performance model. The input parameters to the performance model for these are shown in Table A1. The cruise altitude, h_{cruise} , for these cases was fixed at 35,000 ft. The TSFC data for different engines were obtained from open sources (<https://www.janes.com/> (accessed on April 2023)) [42].

Table A1. Input parameters of the aircraft performance model used for validation.

Aircraft	Cruise Mach No.	Cruise Distance	Cruise Fuel Weight	Operating Empty Weight	Apparent Payload Weight	Lift-to-Drag Ratio	Thrust-Specific Fuel Consumption
	M	d_{cruise}	$W_{f,cruise}$	OEW	$W_{app.payload}$	L/D	TSFC
	(-)	(km)	(kg)	(kg)	(kg)	(-)	(kg/Ns)
A300-600R	0.8	4587	27,852	89,813	32,519.23	15.51	1.637×10^{-5}
A340-642	0.82	13,405	127,337	181,100	45,015.38	19	1.526×10^{-5}
B767-300ERW	0.82	10,619	59,168	93,032	30,636.48	18.31	1.632×10^{-5}

Appendix A.2. PIANO Simulations of the A320neo Aircraft for TAPS-II Exponent Determination

Table A2 shows the details of the PIANO-X simulation of the A320neo aircraft under design range and standard payload conditions. The $EINO_x$ from these simulations has been used to obtain the FAR exponent for the P3–T3 correlation, which is used to calculate the NO_x emissions for the TAPS-II configurations.

Table A2. Cruise condition data for the A320neo in the design range and under standard payload conditions, obtained from PIANO-X.

Cruise Operating Conditions	Cruise Distance (Km)	$W_{f,cruise}$ (kg)	WNO_x (g)	$EINO_x$ (g/kg fuel)
$h_{cruise} = 34,000$ ft Mach no. = 0.775	1025.1	2920.4	16.79	5.75
$h_{cruise} = 36,000$ ft Mach no. = 0.775	2906.41	7703.3	43.07	5.6
$h_{cruise} = 38,000$ ft Mach no. = 0.775	2110.6	5115	27.20	5.32

References

1. Lee, D.S.; Fahey, D.W.; Skowron, A.; Allen, M.R.; Burkhardt, U.; Chen, Q.; Doherty, S.J.; Freeman, S.; Forster, P.M.; Fuglestvedt, J. The contribution of global aviation to anthropogenic climate forcing for 2000 to 2018. *Atmos. Environ.* **2021**, *244*, 117834. [[CrossRef](#)] [[PubMed](#)]
2. Wilcox, L.J.; Shine, K.P.; Hoskins, B.J. Radiative forcing due to aviation water vapour emissions. *Atmos. Environ.* **2012**, *63*, 1–13. [[CrossRef](#)]
3. Stevenson, D.S.; Doherty, R.M.; Sanderson, M.G.; Collins, W.J.; Johnson, C.E.; Derwent, R.G. Radiative forcing from aircraft NOx emissions: Mechanisms and seasonal dependence. *J. Geophys. Res. Atmos.* **2004**, *109*, D17. [[CrossRef](#)]
4. Köhler, M.O.; Rädcl, G.; Shine, K.P.; Rogers, H.L.; Pyle, J.A. Latitudinal variation of the effect of aviation NOx emissions on atmospheric ozone and methane and related climate metrics. *Atmos. Environ.* **2013**, *64*, 1–9. [[CrossRef](#)]
5. Dahlmann, K.; Grewe, V.; Frömming, C.; Burkhardt, U. Can we reliably assess climate mitigation options for air traffic scenarios despite large uncertainties in atmospheric processes? *Transp. Res. Part D Transp. Environ.* **2016**, *46*, 40–55. [[CrossRef](#)]
6. Kärcher, B. Formation and radiative forcing of contrail cirrus. *Nat. Commun.* **2018**, *9*, 1824. [[CrossRef](#)]
7. Schumann, U.; Graf, K. Aviation-induced cirrus and radiation changes at diurnal timescales. *J. Geophys. Res. Atmos.* **2013**, *118*, 2404–2421. [[CrossRef](#)]
8. Burkhardt, U.; Kärcher, B. Global radiative forcing from contrail cirrus. *Nat. Clim. Chang.* **2011**, *1*, 54. [[CrossRef](#)]
9. Heymsfield, A.; Baumgardner, D.; DeMott, P.; Forster, P.; Gierens, K.; Kärcher, B. Contrail Microphysics. *Bull. Am. Meteorol. Soc.* **2010**, *91*, 465–472. [[CrossRef](#)]
10. Burkhardt, U.; Bock, L.; Bier, A. Mitigating the contrail cirrus climate impact by reducing aircraft soot number emissions. *npj Clim. Atmos. Sci.* **2018**, *1*, 37. [[CrossRef](#)]
11. Lacis, A.A.; Schmidt, G.A.; Rind, D.; Ruedy, R.A. Atmospheric CO₂: Principal Control Knob Governing Earth's Temperature. *Science* **2010**, *330*, 356–359. [[CrossRef](#)] [[PubMed](#)]
12. Frömming, C.; Grewe, V.; Brinkop, S.; Jöckel, P.; Haslerud, A.S.; Rosanka, S.; van Manen, J.; Matthes, S. Influence of the actual weather situation on aviation climate effects: The REACT4C Climate Change Functions. *Atmos. Chem. Phys.* **2021**, *21*, 9151–9172. [[CrossRef](#)]
13. Gauss, M.; Isaksen, I.S.A.; Lee, D.S.; Søvde, O.A. Impact of aircraft NOx emissions on the atmosphere tradeoffs to reduce the impact. *Atmos. Chem. Phys.* **2006**, *6*, 1529–1548. [[CrossRef](#)]
14. Advisory Council for Aviation Research and Innovation (ACARE). *Flight 2050 Europe's Vision for Aviation*; European Commission: Brussels, Belgium, 2011.
15. Grewe, V.; Gangoli Rao, A.; Grönstedt, T.; Xisto, C.; Linke, F.; Melkert, J.; Middel, J.; Ohlenforst, B.; Blakey, S.; Christie, S.; et al. Evaluating the climate impact of aviation emission scenarios towards the Paris agreement including COVID-19 effects. *Nat. Commun.* **2021**, *12*, 3841. [[CrossRef](#)] [[PubMed](#)]
16. United Nations Framework Convention on Climate Change (UNFCCC). *Adoption of the Paris Agreement*; United Nations: New York, NY, USA, 2015.
17. Kyrianiadis, K.G.; Dahlquist, E. On the trade-off between aviation NOx and energy efficiency. *Appl. Energy* **2017**, *185*, 1506–1516. [[CrossRef](#)]
18. Yin, F.; Rao, A.G. Performance analysis of an aero engine with inter-stage turbine burner. *Aeronaut. J.* **2017**, *121*, 1605–1626. [[CrossRef](#)]
19. Thoma, E.M.; Grönstedt, T.; Zhao, X. Quantifying the Environmental Design Trades for a State-of-the-Art Turbofan Engine. *Aerospace* **2020**, *7*, 148. [[CrossRef](#)]
20. Perpignan, A.A.V.; Talboom, M.G.; Levy, Y.; Rao, A.G. Emission Modeling of an Interturbine Burner Based on Flameless Combustion. *Energy Fuels* **2018**, *32*, 822–838. [[CrossRef](#)]
21. Sehra, A.K.; Whitlow, W. Propulsion and power for 21st century aviation. *Prog. Aerosp. Sci.* **2004**, *40*, 199–235. [[CrossRef](#)]
22. Freeman, S.; Lee, D.S.; Lim, L.L.; Skowron, A.; De León, R.R. Trading off Aircraft Fuel Burn and NOx Emissions for Optimal Climate Policy. *Environ. Sci. Technol.* **2018**, *52*, 2498–2505. [[CrossRef](#)]
23. Durdina, L.; Brem, B.T.; Setyan, A.; Siegerist, F.; Rindlisbacher, T.; Wang, J. Assessment of Particle Pollution from Jetliners: From Smoke Visibility to Nanoparticle Counting. *Environ. Sci. Technol.* **2017**, *51*, 3534–3541. [[CrossRef](#)] [[PubMed](#)]
24. Kaiser, S.; Schmitz, O.; Ziegler, P.; Klingels, H. The Water-Enhanced Turbofan as Enabler for Climate-Neutral Aviation. *Appl. Sci.* **2022**, *12*, 12431. [[CrossRef](#)]
25. Kaiser, S.; Seitz, A.; Donnerhack, S.; Lundbladh, A. Composite Cycle Engine Concept with Hectopressure Ratio. *J. Propuls. Power* **2016**, *32*, 1413–1421. [[CrossRef](#)]
26. Owen, B.; Anet, J.G.; Bertier, N.; Christie, S.; Cremaschi, M.; Dellaert, S.; Edebeli, J.; Janicke, U.; Kuenen, J.; Lim, L.; et al. Review: Particulate Matter Emissions from Aircraft. *Atmosphere* **2022**, *13*, 1230. [[CrossRef](#)]
27. Stickles, R.; Barrett, J. *TAPS II Technology Final Report—Technology Assessment Open Report*. DTFAWA-10-C-00046, Washington DC, USA, 2013. Available online: https://www.faa.gov/sites/faa.gov/files/about/office_org/headquarters_offices/apl/TAPS_II_Public_Final_Report.pdf (accessed on 1 October 2023).
28. Grewe, V.; Stenke, A. AirClim: An efficient tool for climate evaluation of aircraft technology. *Atmos. Chem. Phys.* **2008**, *8*, 4621–4639. [[CrossRef](#)]

29. Norman, P.D.; Lister, D.H.; Lecht, M.; Madden, P.; Park, K.; Penanhoat, O.; Plaisance, C.; Renger, K. *Development of the Technical Basis for a New Emissions Parameter Covering the Whole Aircraft Operation: NEPAIR*; Final Technical Report No. NEPAIR/WP4/WPR/01; European Commission: Luxembourg, 2003.
30. Schäfer, M.; Strohmeier, M.; Lenders, V.; Martinovic, I.; Wilhelm, M. Bringing up OpenSky: A large-scale ADS-B sensor network for research. In Proceedings of the IPSN-14 Proceedings of the 13th International Symposium on Information Processing in Sensor Networks, Berlin, Germany, 15–17 April 2014; pp. 83–94.
31. Sun, J.; Hoekstra, J.M.; Ellerbroek, J. OpenAP: An Open-Source Aircraft Performance Model for Air Transportation Studies and Simulations. *Aerospace* **2020**, *7*, 104. [[CrossRef](#)]
32. Anderson, J.D.; Bowden, M.L. *Introduction to Flight*; McGraw-Hill Education: New York, NY, USA, 2021.
33. Visser, W.; Broomhead, M. *GSP: A Generic Object-Oriented Gas Turbine Simulation Environment*; National Aerospace Laboratory NLR: Amsterdam, The Netherlands, 2000.
34. Antoine, N.E.; Kroo, I.M. Aircraft optimization for minimal environmental impact. *J. Aircr.* **2004**, *41*, 790–797. [[CrossRef](#)]
35. Döpelheuer, A.; Lecht, M. Influence of engine performance on emission characteristics. RTO AVT Symposium on Gas Turbine Engine Combustion, Emissions and Alternative Fuels. Lisbon, Portugal, 12–16 October; 1998. Available online: <https://api.semanticscholar.org/CorpusID:97575598> (accessed on 1 October 2023).
36. Foust, M.; Thomsen, D.; Stickles, R.; Cooper, C.; Dodds, W. Development of the GE Aviation Low Emissions TAPS Combustor for Next Generation Aircraft Engines. In Proceedings of the 50th AIAA Aerospace Sciences Meeting Including the New Horizons Forum and Aerospace Exposition, Nashville, Tennessee, 9–12 January 2012. [[CrossRef](#)]
37. Megill, L.; Deck, K.; Grewe, V. A systematic approach to select a suitable climate metric for aviation policy and aircraft design. 2023; *preprint*. [[CrossRef](#)]
38. Meinshausen, M.; Nicholls, Z.R.J.; Lewis, J.; Gidden, M.J.; Vogel, E.; Freund, M.; Beyerle, U.; Gessner, C.; Nauels, A.; Bauer, N.; et al. The shared socio-economic pathway (SSP) greenhouse gas concentrations and their extensions to 2500. *Geosci. Model Dev.* **2020**, *13*, 3571–3605. [[CrossRef](#)]
39. Kroon, R. Aviation Emission Inventory: A Contemporized Bottom-Up Emission Inventory for the Year 2019. Master's Thesis, Delft University of Technology, Delft, The Netherlands, 2022.
40. Lefebvre, A.H.; Ballal, D.R. *Gas Turbine Combustion: Alternative Fuels and Emissions*, 3rd ed.; CRC Press: Boca Raton, FL, USA, 2010.
41. Warnatz, J.; Maas, U.; Dibble, R.W. *Combustion: Physical and Chemical Fundamentals, Modeling and Simulation, Experiments, Pollutant Formation*, 4th ed.; Springer: Berlin/Heidelberg, Germany, 2006.
42. Jenkinson, L.R.; Simpkin, P.; Rhodes, D.; Royce, R. *Civil Jet Aircraft Design*; Arnold: London, UK, 1999; Volume 338.

Disclaimer/Publisher's Note: The statements, opinions and data contained in all publications are solely those of the individual author(s) and contributor(s) and not of MDPI and/or the editor(s). MDPI and/or the editor(s) disclaim responsibility for any injury to people or property resulting from any ideas, methods, instructions or products referred to in the content.